European Journal of Mechanics / A Solids 102 (2023) 105117

Contents lists available at ScienceDirect

European Journal of Mechanics / A Solids

journal homepage: www.elsevier.com/locate/ejmsol

Coupling effect of strain gradient strengthening and thermal softening on the microscale plastic behavior of metallic materials

Yanwei Liu [a,*], Hao Long [a], Siyuan Zhang [b], Jingru Song [c], Qianqian Zhou [a], Yueguang Wei [a]

[a] Department of Mechanics and Engineering Science, College of Engineering, BIC-ESAT, Peking University, Beijing, 100871, PR China
[b] School of Mechanical Engineering, University of Shanghai for Science and Technology, Shanghai, 200093, PR China
[c] State-Key Laboratory of Nonlinear Mechanics, Institute of Mechanics, Chinese Academy of Sciences, Beijing, 100190, PR China

ARTICLE INFO

Keywords:
Thermo-mechanical coupled
Microscale plasticity model
Plastic strain gradient
Radial return method
Staggered solution scheme

ABSTRACT

Size effects and thermal effects together determine the microscale plastic response of metallic structures in high-integrated microelectromechanical systems (MEMS) at different temperatures. To investigate the microscale plastic behavior of metallic materials at different temperatures, a thermo-mechanical coupled microscale plasticity model is developed. In the mechanical part of this model, the framework of conventional plasticity theory is maintained, and the plastic strain gradient is introduced as an internal variable to increase the tangential hardening modulus without the introduction of higher-order stress and higher-order boundary conditions. The influence of temperature on the mechanical parameters (e.g. the yield strength) is calibrated by experiment results. In the thermal part of this model, the heat generation in the plastic deformation stage is calculated by the difference between the plastic work and the hardening stored energy influenced by the plastic strain gradient. Due to the strong nonlinearity of the coupled equations, a finite element solution algorithm that combines the radial return method and the staggered solution scheme is proposed. The effectiveness of this model and its solution algorithm is verified by comparisons with the experiment results and a numerical benchmark example. Finally, taking the tensile behavior of a plate with a hole in its center as an example, the coupling effect of strain gradient strengthening and thermal softening on the microscale plastic behavior of metallic materials is investigated. The results show that the microscale plastic behavior of metallic materials at high temperatures depends on the competition between thermal softening and strain gradient strengthening. Our study provides a theoretical basis and a reliable simulation method for the design of MEMS at different temperatures.

1. Introduction

Due to their characteristics of lightweight, low energy consumption, and stable performance, MEMS have a wide range of applications in the fields of aerospace (Javed et al., 2019), deep earth exploration (Middlemiss et al., 2016), advanced manufacturing (Galetto et al., 2019), and so on. The microscale mechanical behaviors of metallic structures in MEMS have a close relationship with the functionality and stability of MEMS. Therefore, the mechanical behaviors of metallic materials at small-scale dimensions have been a hot research topic during the last few years (Askari et al., 2015; Chen et al., 2019; Tajalli, 2020; Tang et al., 2019). Different from the mechanical properties of metallic materials at the macroscale, those, especially the plastic behaviors, at the microscale will show a strong size dependence because of the influences of microstructure evolutions (Lu et al., 2019, 2020; Zhang et al., 2018a, 2018b). For example, when the copper wire diameter is reduced from 50 μm to 20 μm, the dimensionless resistance increases by about 1.7 times (Liu and Dunstan, 2017). In addition to size effects, thermal effects on the plastic behavior of metallic materials at the microscale also cannot be ignored (Farokhi and Ghayesh, 2017; Velayarce et al., 2018; Wheeler et al., 2013). The heat accumulation in the work of MEMS devices and the extreme service environment can cause the temperature inside the device to rise significantly. An increase in temperature can cause changes in material properties (e.g. the yield strength) and leads to thermal stress, which affects the accuracy and service life of the device (Zhang et al., 2019). To optimize the design of MEMS and ensure their reliability across varying temperatures, it is crucial to accurately describe the microscale plastic behavior of metallic structures under the coupling influence of size effects and thermal effects.

In the early stage, researchers only pay attention to the size effect of

* Corresponding author.
E-mail address: yanwei-liu@pku.edu.cn (Y. Liu).

https://doi.org/10.1016/j.euromechsol.2023.105117
Received 27 March 2023; Received in revised form 6 August 2023; Accepted 22 August 2023
Available online 25 August 2023

the plastic behavior of metallic materials at the microscale (Chen and Wang, 2000; Danas et al., 2012; Dunstan and Bushby, 2013; Fleck and Hutchinson, 2001; Lin et al., 2016; Liu et al., 2013; Ran et al., 2013; Zhang et al., 2018a). The conventional theory based on local assumptions has no length parameter, so it cannot predict the influence of structure size on the mechanical response in the stage of plastic deformations. To describe the size-dependent plastic behavior, the strain gradient plasticity theories, in which additional internal variables are introduced to reflect the microstructure interactions, are proposed by previous researchers. According to whether the constitutive equation contains higher-order stress or whether additional boundary conditions are required in the calculation, the strain gradient plasticity theory can be divided into higher-order theory and lower-order theory. In terms of the higher-order theory, Fleck and Hutchinson (2001) established a phenomenological strain gradient plasticity theory (F–H theory) containing two material length parameters: one length parameter is for the case where the stretch gradients are dominant, and the other one is for the problems when the rotation gradients (or shearing gradients) are controlling. Gudmundson (2004) and Gurtin & Anand (Gurtin and Anand, 2009) noted that under some straining history, the F–H theory would violate the thermodynamic requirement, and they gave another alternative formulation to meet the thermodynamic dissipation requirement. After that, Fleck et al. (2014) pointed out that this formulation given by Gurtin and Anand would lead to a discontinuous change of the higher-order stress due to arbitrary small load changes, and they modified the constitutive relations of the F–H theory to satisfy the thermodynamic requirement (Fleck et al., 2015; Hutchinson, 2012). Following their works, many other versions of phenomenological strain gradient plasticity theories were proposed and improved, see examples (Anand et al., 2012; Fleck and Willis, 2009; Miehe et al., 2013; Nielsen and Niordson, 2014; Polizzotto, 2009; Reddy et al., 2008; Voyiadjis et al., 2014). Apart from the pure phenomenological theories of gradient plasticity, strain gradient-enhanced models based on the dislocation flow in crystals are also established (Bittencourt, 2018; Gurtin and Reddy, 2014; Jebahi et al., 2020; Ryś et al., 2022; Scherer et al., 2019; Wulfinghoff and Böhlke, 2015). Because the higher-order theory needs additional boundary conditions, there are great difficulties in numerical realization and engineering application. In contrast, the lower-order theory maintains the framework of traditional plasticity and is easier to apply. Many researchers have conducted in-depth studies on the lower-order strain gradient plasticity theory. Based on the thermodynamic principle, the possibility of a model of non-local plasticity in the absence of higher-order stresses or higher-order boundary conditions is examined by Acharya and Shawki (1995), and they concluded that the thermodynamic restriction does not preclude the existence of a class of second-deformation-gradient-dependent plastic constitutive relationship. Acharya and Bassani (2000) pointed out that without changing the theoretical framework of J_2 plasticity, the only possible formulation is a flow theory with strain gradient effects represented as an internal variable to increase the current tangent hardening modulus. Inspired by the work of Acharya and Bassani, Chen and Wang (2000) proposed a specific hardening relationship and developed a lower-order strain gradient plasticity theory (C–W theory). Following the framework of mechanism-based strain gradient plasticity (MSG) (Gao et al., 1999), Huang et al. (2004) established a conventional theory of mechanism-based strain gradient plasticity (CMSG), and they concluded that the difference between CMSG and MSG is only significant within a thin boundary layer. Although the mathematical expressions of CMSG and C–W theory are different, they are essentially the same, that is, the strain gradient increases the instantaneous plastic tangent modulus. It is noted that there is a large discontinuity in plastic strain gradient in both theories. Acharya et al. (2004) investigated the boundary conditions and plastic strain-gradient discontinuity in lower-order gradient plasticity, and the results showed that the lower-order theory can accommodate the higher-order boundary conditions and there seems to be no adverse consequences of a discontinuity in the gradient of plastic strain. In addition, lower-order strain gradient plasticity theories based on the evolution of dislocation in crystals were also developed (Acharya and Beaudoin, 2000; Arora et al., 2023; Demiral et al., 2014; Haouala et al., 2020; Xiao et al., 2019), and these theories successfully described the plastic deformation of metal polycrystals (Beaudoin et al., 2000), the fracture behaviors of ductile single crystals and the interface of a bicrystal with symmetric tilt boundary (Tang et al., 2004, 2005), and so on.

With the development of study and the increase of actual needs of engineering, researchers further pay attention to thermal effects on the basis of focusing on size effects (Faghihi and Voyiadjis, 2014; Voyiadjis and Faghihi, 2012; Voyiadjis et al., 2014; Wu et al., 2003). Wu et al. (2003) incorporated thermal effects into MSG to reconstruct the constitutive laws and examined the combined effect of strain gradient and temperature on the dynamic growth of voids. Voyiadjis and Faghihi (2012) developed a thermo-mechanical coupled strain gradient plasticity theory with energetic and dissipative length scales and investigated the mechanical behavior of a thin film on an elastic substrate under biaxial straining. In this context, Forest and Aifantis (2010) discussed some links between recent gradient thermo-elasto-plasticity theories and the thermo-mechanics of generalized continua, and Bertram and Forest (2014) proposed an anisotropic model of strain gradient thermo-plasticity. In addition, Wcisło and Pamin (2017) established a gradient-enhanced thermo-mechanical model, in which the higher-order gradients of the temperature field are incorporated. Aldakheel and Miehe (2017) extended the gradient plasticity model of Miehe (Miehe et al., 2013) to account for the thermal effect under small deformations and finite deformations in the logarithmic strain space and developed two classes of solution schemes (Global product formula algorithm and implicit coupled algorithm) for this coupled problem. Most of the thermo-mechanical coupled strain gradient plasticity theories mentioned above are based on the higher-order theory. Due to the existence of higher-order stress or additional boundary conditions, the framework of these theories is different from that of traditional J_2 plasticity theory, which leads to difficulties in numerical realization and engineering application. In addition, with regard to the thermo-mechanical coupled response of metallic materials at the microscale, most studies focus on the influence of strain gradient on the plastic hardening and heat generation, but neglect the combined effect of strain gradient and temperature on the plasticity of microscale metallic materials under high temperatures. Therefore, it is necessary to develop a thermo-mechanical coupled microscale plasticity model based on the lower-order theory and investigate the couple effect of strain gradient and temperature.

In this work, the thermal effect is incorporated into the C–W theory (Chen and Wang, 2000) to construct a new thermo-mechanical coupled microscale plasticity model and the combined effect of strain gradient strengthening and thermal softening on the plasticity of metallic materials at the microscale is investigated. What should be emphasized is that our model realizes the coupling of strain gradient effect and thermal effect under the framework of traditional J_2 plasticity theory, which is very beneficial for practical applications and numerical implementation. This paper is organized as follows: Section 2 outlines the framework of the thermo-mechanical coupled microscale plasticity model. In Section 3, the finite element solution algorithm of this model is developed by combining the staggered solution scheme and the radial return method. The effectiveness of this model and its numerical implementation is validated by comparisons with the experiment results, and the coupling

effect of strain gradient and temperature on the microscale plasticity of metallic materials is analyzed in Section 4. In Section 5, the main conclusions are summarized.

2. Theory

The thermo-mechanical coupled microscale plasticity model presented here stands on the C–W strain gradient plasticity model. Firstly, the kinematics are presented in Section 2.1. Secondly, in Section 2.2, the balance equations and boundary conditions of this model are introduced in detail. Then, the constitutive equations are described in Section 2.3. Finally, the control equations, boundary conditions, and initial conditions are concluded.

2.1. Kinematics

The proposed theoretical framework refers to an elastic-plastic solid occupying a domain $\Omega \subset \Re^d (d = 1, 2, 3)$ with an external boundary $\partial\Omega \subset \Re^{d-1}$, and the outward unit normal vector of the boundary is denoted as $\boldsymbol{n}$. The coordinate of an arbitrary material point in the elastic-plastic solid is set as $\boldsymbol{X}$ and the kinematic variables (the displacement and the temperature) at time t can be expressed as $\boldsymbol{u}(\boldsymbol{X}, t)$ and $\theta(\boldsymbol{X}, t)$. The framework of the thermo-mechanical coupled microscale plasticity model is limited to the isotropic and small deformation conditions. The total strain tensor $\boldsymbol{\varepsilon}$ is defined as

$$\boldsymbol{\varepsilon} = \frac{1}{2}(\nabla \boldsymbol{u} + \boldsymbol{u}\nabla) \tag{1}$$

For the thermo-plastic problem, the elastic strain tensor $\boldsymbol{\varepsilon}^e$ is obtained in an additive format from the total strain $\boldsymbol{\varepsilon}$, the plastic strain $\boldsymbol{\varepsilon}^p$, and the thermal strain $\boldsymbol{\varepsilon}^\theta$:

$$\boldsymbol{\varepsilon}^e = \boldsymbol{\varepsilon} - \boldsymbol{\varepsilon}^p - \boldsymbol{\varepsilon}^\theta \tag{2}$$

where $\boldsymbol{\varepsilon}^p$ is a symmetric second-order tensor and starts to evolve from the initial condition $\boldsymbol{\varepsilon}^p(X, t) = 0$, and $\boldsymbol{\varepsilon}^\theta$ is a spherical second-order tensor and can be calculated by

$$\boldsymbol{\varepsilon}^\theta = \alpha(\theta - \theta_0)\boldsymbol{I} \tag{3}$$

where α is the coefficient of thermal expansion, θ is the current temperature, θ_0 is the initial temperature, and $\boldsymbol{I}$ is the unit second-order tensor.

2.2. Balance equations and boundary conditions

The balance equations of thermo-plastic problems are composed of the force field balance equation and the thermal field balance equation. Firstly, the balance equation of the force field is given based on the balance of linear momentum in Section 2.2.1. Then, the balance equation of the thermal field that accounts for the influence of strain gradient is introduced in Section 2.2.2.

2.2.1. Force field equation

Under the static and physical conditions, the balance of linear momentum of arbitrary subdomains Ω_{sub} in the elastic-plastic solid can be expressed as

$$\int_{\Omega_{\text{sub}}} \boldsymbol{t}_{\text{sub}} dS_{\text{sub}} = 0 \tag{4}$$

where $\boldsymbol{t}_{\text{sub}}$ is the surface force on the boundary S_{sub} of the subdomain Ω_{sub}. Herein, the body force is neglected. Based on the Gauss theorem, the local form of Eq. (4) is

$$\nabla \cdot \boldsymbol{\sigma} = 0 \tag{5}$$

where $\boldsymbol{\sigma}$ is the Cauchy stress tensor. The Dirichlet- and Neuman-conditions for the deformation and the external traction on the boundary are

$$\boldsymbol{u} = \boldsymbol{u}_0 \text{ on} \partial\Omega^u \tag{6a}$$

$$\boldsymbol{\sigma} \cdot \boldsymbol{n} = \boldsymbol{t} \text{ on} \partial\Omega^T \tag{6b}$$

2.2.2. Thermal field equation

The local form of the first law of thermodynamics that holds at every point in the elastic-plastic solid reads

$$\rho\dot{\Theta} = \dot{\boldsymbol{\varepsilon}} : \boldsymbol{\sigma} + r - \nabla \cdot \boldsymbol{q} \tag{7}$$

where ρ denotes the density of the material, Θ is the internal energy per unit mass, r is the amount of heat supply per unit time and unit volume, and $\boldsymbol{q}$ is the heat flux vector. Here, $\boldsymbol{q}$ is given by Fourier's law of heat conduction $\boldsymbol{q} = -k\nabla\theta$, where k is the thermal conductivity. The internal energy per unit mass Θ can be obtained in an additive format from Helmholtz's free energy ψ and the product of entropy s and temperature θ:

$$\Theta = \psi + s\theta \tag{8}$$

Using Eq. (8) in Eq. (7), one can get

$$\rho\left(\dot{\Psi} + \dot{s}\theta + s\dot{\theta}\right) = \dot{\boldsymbol{\varepsilon}} : \boldsymbol{\sigma} + r - \nabla \cdot \boldsymbol{q} \tag{9}$$

In our work, the main purpose is to construct the thermo-mechanical coupled microscale plasticity model based on the lower-order theory. The higher-order stress will be neglected, and the effect of the strain gradient on plasticity is introduced by increasing the plastic tangent modulus. In the traditional case, the balance equation of the thermal field can be written as (the detailed derivation can be found in Appendix)

$$\rho c_\varepsilon \dot{\theta} = k\nabla^2\theta + r - \theta \boldsymbol{D} : \alpha I : \left(\dot{\boldsymbol{\varepsilon}} - \dot{\boldsymbol{\varepsilon}}^p\right) + \boldsymbol{\sigma} : \dot{\boldsymbol{\varepsilon}}^p - K\dot{\bar{\varepsilon}}^p \tag{10}$$

where $c_\varepsilon = -\theta\partial^2\Psi/\partial\theta^2$ is the specific heat capacity, $\boldsymbol{D}$ is the fourth-order elastic tensor, and K is the thermodynamic force that is energy conjugated to the effective plastic strain $\bar{\varepsilon}^p$. $\bar{\varepsilon}^p$ can be calculated by $\bar{\varepsilon}^p = \int \dot{\bar{\varepsilon}}^p dt$ and $\dot{\bar{\varepsilon}}^p = \sqrt{2(\dot{\boldsymbol{\varepsilon}}^p : \dot{\boldsymbol{\varepsilon}}^p)}/3$. In the traditional J_2 plasticity flow theory, K reads

$$K(\bar{\varepsilon}^p) = \int_0^{\bar{\varepsilon}^p} A'(\beta) d\beta \tag{11}$$

where $A'(\beta)$ is the tangent hardening modulus. In order to consider the effect of strain gradient without introducing the higher-order stress, the strain gradient term is used as a correction parameter to correct K referring to the previous work (Chen and Wang, 2001). When the strain gradient effect is introduced into K, K is

$$K(l\eta, \bar{\varepsilon}^p) = \int_0^{\bar{\varepsilon}^p} A'(\beta) g(l\eta, \beta) d\beta \tag{12}$$

where $g(l\eta, \beta)$ is the correction term that considers the effect of strain gradients, and its detailed form will be introduced in Section 2.3. What needs to be emphasized is that Eq. (12) can not be integrated analytically due to the reason that the strain gradient term η varies with the gradient of the effective plastic strain under a complex state of stress. In previous research, it also appears in the form of an integral (Ban et al.,

2017). At this time, the balance equation of the thermal field reads

$$\rho c_\varepsilon \dot{\theta} = k\nabla^2\theta + r - \theta \boldsymbol{D} : \alpha \boldsymbol{I} : \left(\dot{\boldsymbol{\varepsilon}} - \dot{\boldsymbol{\varepsilon}}^p\right) + \boldsymbol{\sigma} : \dot{\boldsymbol{\varepsilon}}^p - \int_0^{\overline{\varepsilon}^p} A^{'}(\beta) g(l\eta, \beta) d\beta \dot{\overline{\varepsilon}}^p \quad (13)$$

The Dirichlet- and Neuman-conditions for the thermal field on the boundary are

$$\theta = \theta_0 \text{ on} \partial\Omega^\theta \quad (14a)$$

$$\boldsymbol{q} \cdot \boldsymbol{n} = h \text{ on} \partial\Omega^h \quad (14b)$$

where h is the heat flux. Eqs. (5), (6), (13) and (14) are the balanced equations and the boundary conditions of the thermo-mechanical coupled microscale plasticity model.

2.3. Constitutive equations

The constitutive equations include three parts: the stress-strain relationship, the yield function, and the evolution law of plastic strain. In Section 2.3.1, the stress-strain relationship is presented first. Then, the yield function adopted in our work is introduced in Section 2.3.2. Finally, the evolution law of plastic strain is described in Section 2.3.3.

2.3.1. The stress-strain relationship

The constitutive equation of the thermo-mechanical coupled microscale plasticity model reads

$$\boldsymbol{\sigma} = \boldsymbol{D} : \left(\boldsymbol{\varepsilon} - \boldsymbol{\varepsilon}^p - \boldsymbol{\varepsilon}^\theta\right) \quad (15)$$

According to the previous experiment results (Seungwoo et al., 2008; Wheeler et al., 2013), it can be known that the influence of temperature on the elastic constant is relatively small when the temperature is not very high. Therefore, the effect of temperature on $\boldsymbol{D}$ is neglected. The incremental form of Eq. (15) is

$$\dot{\boldsymbol{\sigma}} = \boldsymbol{D} : \left(\dot{\boldsymbol{\varepsilon}} - \dot{\boldsymbol{\varepsilon}}^p - \dot{\boldsymbol{\varepsilon}}^\theta\right) \quad (16)$$

2.3.2. The yield function

On the premise of meeting the thermodynamic limitations and maintaining the traditional form of J_2 plasticity theory, Acharya and Bassani (2000) pointed out that the only possible form to realize the gradient plastic strengthening is a flow theory represented as an internal variable that plays a role in increasing the plastic tangential modulus. Following their viewpoint, Chen and Wang (2001) proposed a specific hardening relationship. In order to introduce the strain gradient effect and avoid the complexity of the theoretical framework, the yield function proposed by Chen and Wang is adopted. The C–W yield function f reads

$$f = \overline{\sigma} - \sigma_{y_0}(\theta) - K \quad (17)$$

where $\overline{\sigma}$ is the effective stress, and $\sigma_{y_0}(\theta)$ is the yield strength. $\overline{\sigma}$ can be calculated by

$$\overline{\sigma} = \sqrt{\frac{3}{2}\boldsymbol{S} : \boldsymbol{S}} \quad (18)$$

where $\boldsymbol{S}$ is the deviatoric part of Cauchy stress $\boldsymbol{\sigma}$, and it can be obtained by $\boldsymbol{S} = \boldsymbol{\sigma} - \boldsymbol{I}\sigma_{ii}/3$. According to the previous experimental results (Seungwoo et al., 2008; Wheeler et al., 2013), it can be known that when the temperature is not extremely high, the influence of temperature on the modulus of metallic materials is small, but it has a significant impact on the yield strength (Ottosen and Ristinmaa, 2005). The relationship between the yield strength and the temperature can be fitted by experiment results. In this paper, a linear softening relationship (e.g. $\sigma_{y_0} = \sigma_{y_0}^{\theta=0} - k_0 \cdot \theta$) is adopted on the premise of accuracy and simplicity. In the C–W yield function, K is written as

$$K(l\eta, \overline{\varepsilon}^p) = \int_0^{\overline{\varepsilon}^p} A^{'}(\beta)\left(1 + \frac{l^2\eta^2}{\beta^2}\right)^\gamma d\beta \quad (19)$$

where l is the intrinsic characteristic length of materials for the rotation gradient, and γ is the exponent. Referring to previous work (Chen and Wang, 2000), the range of γ is 0–1, and in our study γ is taken to as 1. η is the plastic strain gradient term, and it is defined as

$$\eta = \sqrt{\left(\frac{l_1}{l}\right)^2 \rho_{ijk}^{(1)} \rho_{ijk}^{(1)} + {\chi_e}^2} \quad (20)$$

with

$$\chi_e = \sqrt{\frac{2}{3}\chi_{ij}\chi_{ij}}, \chi_{ij} = e_{its}\rho_{jts}, \rho_{jts} = \varepsilon_{jt,s}^p \quad (21)$$

where l_1 is the intrinsic characteristic length of materials for the stretch gradient, $\rho_{ijk}^{(1)}$ is the stretch gradient tensor, χ_e is the effective rotation gradient, and ρ_{nts} is the gradient of the plastic strain. $\rho_{ijk}^{(1)}$ can be calculated by (Fleck and Hutchinson, 2001)

$$\rho_{ijk}^{(1)} = \rho_{ijk}^S - \frac{1}{5}\left(\delta_{ij}\rho_{kpp}^S + \delta_{kj}\rho_{ipp}^S + \delta_{ik}\rho_{jpp}^S\right) \quad (22)$$

where $\rho_{ijk}^S = \frac{1}{3}(\rho_{ijk} + \rho_{jki} + \rho_{kij})$ is the 'symmetrical' part of ρ_{nts}.

2.3.3. The evolution law of plastic strain

According to the second law of thermodynamics, mechanical dissipation needs to satisfy the inequality:

$$\gamma_{mech} \equiv \sigma_{ij}\dot{\underset{ij}{e}}\, p - K\dot{\overline{\varepsilon}}^p \geq 0 \quad (23)$$

In addition, the yield function $f(\sigma_{ij}, K)$ is always less than or equal to zero. Following the postulate of maximum dissipation, the evolution law of plastic strain can be obtained by minimizing $-\gamma_{mech}$ under the constraint that $f(\sigma_{ij}, K) \leq 0$. Herein, the yield function is assumed to be a convex function of σ_e and K. The Lagrange function of this problem is defined as

$$L\left(\sigma_{ij}, K, \dot{\lambda}\right) = -\sigma_{ij}\dot{\underset{ij}{e}}\, p + K\dot{\overline{\varepsilon}}^p + \dot{\lambda} f\left(\sigma_{ij}, K\right) \quad (24)$$

where $\dot{\lambda}$ is a Lagrange multiplier. Following the equations

$$\frac{\partial L}{\partial \sigma_{ij}} = 0, \frac{\partial L}{\partial K} = 0 \quad (25)$$

the evolution law of the plastic strain can be obtained:

$$\dot{\underset{ij}{e}}\, p = \dot{\lambda}\frac{\partial f}{\partial \sigma_{ij}}, \dot{\overline{\varepsilon}}^p = -\dot{\lambda}\frac{\partial f}{\partial K} \quad (26)$$

Based on Eqs. (17) and (26), it can be known that the Lagrange multiplier $\dot{\lambda}$ is equal to the effective plastic strain $\dot{\overline{\varepsilon}}^p$.

Finally, the thermo-mechanical coupled microscale plasticity model can be described as follows. The governing equations are

$$
\begin{cases}
\nabla\cdot\boldsymbol{\sigma} = 0 \\
\boldsymbol{\sigma} = \boldsymbol{D} : \left(\boldsymbol{\varepsilon} - \boldsymbol{\varepsilon}^{p} - \boldsymbol{\varepsilon}^{\theta}\right) \\
\rho c_{\varepsilon}\dot{\theta} = k\nabla^{2}\theta + r - \theta\boldsymbol{D} : \alpha I : \left(\dot{\boldsymbol{\varepsilon}} - \dot{\boldsymbol{\varepsilon}}^{p}\right) + \boldsymbol{\sigma}
\end{cases}
$$

$$
\dot{\boldsymbol{\varepsilon}}^{p} - K\dot{\bar{\varepsilon}}^{p}\boldsymbol{\varepsilon}, \boldsymbol{\varepsilon}^{e} = \boldsymbol{\varepsilon} - \boldsymbol{\varepsilon}^{p} - \boldsymbol{\varepsilon}^{\theta}, \boldsymbol{\varepsilon}^{\theta} = \alpha(\theta - \theta_{0})\boldsymbol{I} f
$$

$$
= \bar{\sigma} - \sigma_{y_0} - K, \dot{\varepsilon}_{ij}^{p} = \dot{\lambda}\frac{\partial f}{\partial \sigma_{ij}}, \dot{\bar{\varepsilon}}^{p} = -\dot{\lambda}\frac{\partial f}{\partial K}\bar{\sigma} = \sqrt{\frac{3}{2}\boldsymbol{S} : \boldsymbol{S}}, \sigma_{y_0}
$$

$$
= \sigma_{y_0}^{\theta=0} - k_{\theta}\cdot\theta, K(l\eta, \bar{\varepsilon}^{p}) = \int_{0}^{\bar{\varepsilon}^{p}} A'(\beta)\left(1 + \frac{l^{2}\eta^{2}}{\beta^{2}}\right)^{\gamma} d\beta\eta
$$

$$
= \sqrt{\left(\frac{l_1}{l}\right)^{2}\rho_{ijk}^{(1)}\rho_{ijk}^{(1)} + \chi_{e}^{2}}, \chi_{e} = \sqrt{\frac{2}{3}\chi_{ij}\chi_{ij}}, \chi_{ij} = e_{its}\rho_{jts}, \rho_{jts} = \varepsilon_{jt,s}^{p}\rho_{ijk}^{(1)}
$$

$$
= \rho_{ijk}^{S} - \frac{1}{5}\left(\delta_{ij}\rho_{kpp}^{S} + \delta_{kj}\rho_{ipp}^{S} + \delta_{ik}\rho_{jpp}^{S}\right), \rho_{ijk}^{S} = \frac{1}{3}\left(\rho_{ijk} + \rho_{jki} + \rho_{kij}\right) \tag{27}
$$

The boundary conditions read

$$
\begin{cases}
\boldsymbol{u} = \boldsymbol{u}_{0} \ \text{on}\partial\Omega^{u} \\
\boldsymbol{\sigma}\cdot\boldsymbol{n} = \boldsymbol{t} \ \text{on}\partial\Omega^{T} \\
\theta = \theta_{0} \ \text{on}\partial\Omega^{\theta} \\
\boldsymbol{q}\cdot\boldsymbol{n} = h \ \text{on}\partial\Omega^{h}
\end{cases} \tag{28}
$$

The initial conditions are specified as

$$
\begin{cases}
\boldsymbol{u}(\boldsymbol{X}, 0) = \boldsymbol{0} \ \text{in}\ \Omega \\
\theta(\boldsymbol{X}, 0) = \theta_{0} \ \text{in}\ \Omega
\end{cases} \tag{29}
$$

3. Numerical implementation

In this section, combining the radial return algorithm and the staggered solution scheme, a numerical implementation strategy of the thermo-mechanical coupled microscale plasticity model is proposed. First, in Section 3.1, the radial return method to implement the C–W strain gradient plasticity model is presented. The staggered solution scheme related to the thermo-plastic problem is described in Section 3.2. Finally, Section 3.3 provides a detailed introduction to the weak formulation and the solving flowchart of the thermo-mechanical coupled microscale plasticity model.

3.1. The radial return method for solving the C–W strain gradient plasticity model

Algorithm 1. The radial return algorithm for the C–W strain gradient plasticity model.

1. Setting the initial value: $k = 0$, $\boldsymbol{\varepsilon}^{p(0)} = \boldsymbol{\varepsilon}_{n}^{p}$, $\bar{\varepsilon}^{p(0)} = \bar{\varepsilon}_{n}^{p}$, $\Delta\lambda^{(0)} = 0$, $\boldsymbol{\sigma}^{(0)} = \boldsymbol{D} : (\boldsymbol{\varepsilon}_{n+1} - \boldsymbol{\varepsilon}_{n+1}^{\theta} - \boldsymbol{\varepsilon}^{p(0)})$, $\boldsymbol{n}^{(0)} = \sqrt{\frac{3}{2}}\frac{\boldsymbol{S}^{(0)}}{\bar{\sigma}^{(0)}}$;
2. Judging whether the system is in balance. If $[F_{system}]_{total} \leq TOL$, the iteration ends. Otherwise, go to step 3;
3. Calculating the correction of effective plastic strain based on Eq. (33);
4. Updating the effective plastic strain increment, the plastic strain, and the stress: $\Delta\lambda^{(k+1)} = \Delta\lambda^{(k)} + \delta\lambda^{(k)}$, $\boldsymbol{\varepsilon}^{p(k+1)} = \boldsymbol{\varepsilon}^{p(k)} + \delta\lambda^{(k)}\boldsymbol{r}_{n+1}$, $\boldsymbol{\sigma}^{(k+1)} = \boldsymbol{\sigma}^{(k)} - 2\mu\delta\lambda^{(k)}\boldsymbol{r}_{n+1}$. Let $k = k+1$, and then go to step 2.

The C–W strain gradient plasticity model maintains the framework of traditional J_2 flow plasticity theory, so the radial return algorithm can be used to implement it numerically. Here, the incremental finite element method is adopted. The deformation, stress, and temperature of step n are known, and they are written as $\boldsymbol{\varepsilon}_{n}, \boldsymbol{\varepsilon}_{n}^{p}, \bar{\varepsilon}_{n}^{p}, \boldsymbol{\sigma}_{n}, u_{n}, \theta_{n}$. Based on the backward Euler method, the stress and strain of step n+1 can be obtained:

$$
\boldsymbol{\varepsilon}_{n+1} = \boldsymbol{\varepsilon}_{n} + \Delta\boldsymbol{\varepsilon} \tag{30a}
$$

$$
\boldsymbol{\varepsilon}_{n+1}^{p} = \boldsymbol{\varepsilon}_{n}^{p} + \Delta\lambda_{n+1}\boldsymbol{r}_{n+1} \tag{30b}
$$

$$
\bar{\varepsilon}_{n+1}^{p} = \bar{\varepsilon}_{n}^{p} + \Delta\lambda_{n+1} \tag{30c}
$$

$$
\boldsymbol{\sigma}_{n+1} = \boldsymbol{D} : \left(\boldsymbol{\varepsilon}_{n+1} - \boldsymbol{\varepsilon}_{n+1}^{\theta} - \boldsymbol{\varepsilon}_{n+1}^{p}\right) \tag{30d}
$$

where $\Delta\boldsymbol{\varepsilon}$ is the incremental strain tensor, and it can be calculated by solving the balance equation of force field (the detailed process can be found in Section 3.3); $\boldsymbol{r}_{n+1}$ is the flow direction tensor of plastic strain, and it reads

$$
\boldsymbol{r}_{n+1} = 3\boldsymbol{S}_{n+1}/2\bar{\sigma}_{n+1} \tag{31}
$$

Using Eqs. (30a), (30b) and (30c) in Eq. (30d), the stress of step n+1 can also be written as

$$
\boldsymbol{\sigma}_{n+1} = \boldsymbol{\sigma}_{n+1}^{0} - \Delta\lambda_{n+1}\boldsymbol{D} : \boldsymbol{\varepsilon}_{n+1}^{p} = \boldsymbol{\sigma}_{n+1}^{0} - \Delta\lambda_{n+1}2\mu\boldsymbol{r}_{n+1} \tag{32}
$$

where $\boldsymbol{\sigma}_{n+1}^{0} = \boldsymbol{D} : (\boldsymbol{\varepsilon}_{n+1} - \boldsymbol{\varepsilon}_{n+1}^{\theta})$ is the elastic predicted stress tensor. It is noted that the flow direction is unchanged during the process of plastic strain correction. Namely, it can be calculated by the elastic predicted stress: $\boldsymbol{r}_{n+1} = 3\boldsymbol{S}_{n+1}^{0}/2\bar{\sigma}_{n+1}^{0}$. In Eqs. (30a), (30b), (30c), and (31), only the incremental plastic strain $\Delta\lambda_{n+1}$ is unknown. Obviously, once $\Delta\lambda_{n+1}$ is obtained, the stress and strain of step n+1 will be known. The incremental plastic strain $\Delta\lambda_{n+1}$ can be obtained by solving the yield function:

$$
f_{n+1} = \bar{\sigma}_{n+1} - \sigma_{y_0} - K(l\eta_{n+1}, \bar{\varepsilon}_{n+1}^{p}) = \bar{\sigma}_{n+1}^{0} - 3\mu\Delta\lambda_{n+1} - \sigma_{y_0} - K(l\eta_{n+1}, \bar{\varepsilon}_{n+1}^{p}) \tag{33}
$$

Eq. (33) is nonlinear, so the Newton iterative method needs to be used to calculate $\Delta\lambda_{n+1}$. It is noted that the forward Euler method is used to calculate η_{n+1}. Namely, η_{n+1} can be obtained based on the plastic strain of step n with Eqs. (20)–(22). At this time, the step needs to be small enough to reduce the calculation error. The derivation of Eq. (33) with respect to $\Delta\lambda_{n+1}$ is

$$
\frac{\partial f_{n+1}}{\partial\Delta\lambda_{n+1}} = 3\mu + E^{p} \tag{34}
$$

where $E^{p} = \partial K/\partial\bar{\varepsilon}^{p}|_{\bar{\varepsilon}^{p}=\bar{\varepsilon}}\boldsymbol{n} + 1^{p}$ is the plastic tangent modulus. Then, in the k-step iteration of the radial return method, the effective plastic strain correction $\delta\lambda^{(k)} = \Delta\lambda^{(k+1)} - \Delta\lambda^{(k)}$ is

$$
\delta\lambda^{(k)} = \frac{f_{n+1}^{(k)}}{3\mu + E^{p(k)}} \tag{35}
$$

The detailed process of the radial return algorithm for solving the C–W strain gradient plasticity model is shown in Algorithm 1.

3.2. The staggered solution scheme for the thermo-plastic problem

When it comes to addressing the thermo-plastic issue, two kinds of solution approaches are available: the simultaneous solution algorithm and the staggered solution scheme. Aldakheel and Miehe (2017) pointed out that the simultaneous solution algorithm arises from high computational efforts in comparison with the staggered solution scheme under the same computational accuracy. Therefore, in this work, the staggered

solution scheme, as shown in Fig. 1, is adopted to solve the thermo-plastic problem. The procedure is as follows: within a time step Δt_n, the temperature field calculated at time t_i is used as an input in the calculation of the force field. The calculation is performed to obtain the displacement field at time t_{i+1}. After that, the displacement field at time t_{i+1} is used as an input in the calculation of the thermal field. The calculation is performed to obtain the thermal field at time t_{i+1}. Then, judging whether the force field equation and the thermal field equation are satisfied at the same time according to the thermal field and displacement field at time t_{i+1}. If it is not, the next iteration is performed. When both the force field equation and the thermal field equation are satisfied, the next time step Δt_{n+1} is performed.

3.3. The weak formulation and the solving flowchart of the thermo-mechanical coupled microscale plasticity model

Based on the principle of virtual work and the balance equation of force field, the weak form of force equation reads

$$\delta\Pi_u = \int_\Omega \sigma_{ij}\delta(\varepsilon_{ij})dV - \int_{\partial\Omega} t_i\delta(u_i)dV = 0 \tag{36}$$

For the analysis of the plastic behavior of materials, the incremental finite element method is usually adopted. Therefore, the incremental form of Eq. (36) needs to be given. If the stress $\sigma_{ij} + \Delta\sigma_{ij}$ and the boundary force $t_i + \Delta t_i$ at the time of $t + \Delta t$ meet the balance equation of force, the total virtual work done by these forces along the virtual displacement $\delta(\Delta u_i)$ that satisfies the geometric equation is zero:

$$\begin{aligned}\delta(\Delta\Pi_u) &= \int_\Omega (\sigma_{ij} + \Delta\sigma_{ij})\delta(\Delta\varepsilon_{ij})dV - \int_{\partial\Omega} (t_i + \Delta t_i)\delta(\Delta u_i)dV \\ &= \int_\Omega \sigma_{ij}\delta(\Delta\varepsilon_{ij})dV + \int_\Omega \Delta\sigma_{ij}\delta(\Delta\varepsilon_{ij})dV - \int_{\partial\Omega} (t_i + \Delta t_i)\delta(\Delta u_i)dV = 0\end{aligned} \tag{37}$$

Eq. (37) will be used to calculate the displacement field. With regard to the thermal field, the weak form can be obtained based on Eq. (13):

$$\delta\Pi_\theta = \int_\Omega \rho c_\varepsilon \dot{\theta}\delta(\theta)dV + \int_\Omega \left[\theta\alpha D_{ijkl}\delta_{kl}\left(\dot{\varepsilon}_{ij} - \dot{\varepsilon}^p_{ij}\right) - r - \sigma_{ij}\dot{\varepsilon}^p_{ij} + K\dot{\bar{\varepsilon}}^p\right]\delta(\theta)dV - \int_\Omega k\theta_{,i}\delta(\theta)dV = 0 \tag{38}$$

Following the backward Euler method, the time-related items in Eq. (38) are discretized as

$$\dot{\theta} = \frac{\theta - \theta^n}{\Delta t}, \dot{\varepsilon}_{ij} = \frac{\varepsilon_{ij} - \varepsilon^n_{ij}}{\Delta t}, \dot{\varepsilon}^p_{ij} = \frac{\varepsilon^p_{ij} - \varepsilon^{p_n}_{ij}}{\Delta t}, \dot{\bar{\varepsilon}}^p = \frac{\bar{\varepsilon}^p - \bar{\varepsilon}^{p_n}}{\Delta t} \tag{39}$$

Using Eq. (39) in Eq. (38), one can obtain

$$\begin{aligned}\delta\Pi_\theta &= \int_\Omega \rho c_\varepsilon \frac{\theta - \theta^n}{\Delta t}\delta(\theta)dV - \int_\Omega \left(k_{ij}\theta_{,j}\right)_{,i}\delta(\theta)dV \\ &+ \int_\Omega \left[\theta\alpha D_{ijkl}\delta_{kl}\left(\frac{\varepsilon_{ij} - \varepsilon^n_{ij}}{\Delta t} - \frac{\varepsilon^p_{ij} - \varepsilon^{p_n}_{ij}}{\Delta t}\right) - r - \sigma_{ij}\frac{\varepsilon^p_{ij} - \varepsilon^{p_n}_{ij}}{\Delta t} + K\frac{\bar{\varepsilon}^p - \bar{\varepsilon}^{p_n}}{\Delta t}\right]\delta(\theta)dV = 0\end{aligned} \tag{40}$$

Eq. (40) will be used to calculate the thermal field.

The numerical solution of the thermo-mechanical coupled microscale plasticity model is implemented using Fenics (Alnæs et al., 2015; Logg et al., 2012). The iterative predictor-corrector return mapping algorithm is embedded in the global loop for restoring equilibrium, and the linear solver is used in our code. The core of the algorithm is the combination of the radial return method and the staggered solution scheme, and the detailed process of the algorithm is shown in Fig. 2.

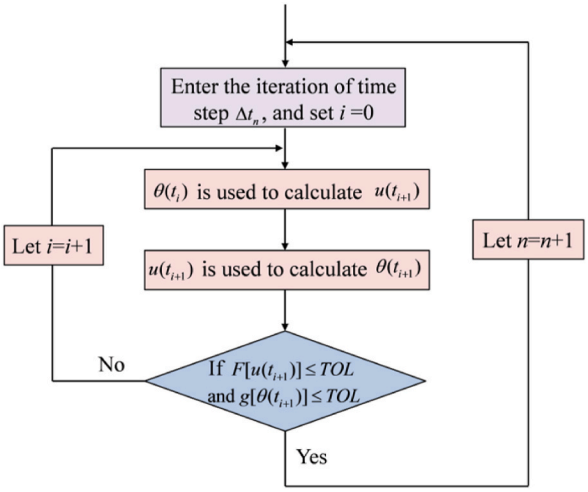

Fig. 1. The staggered process for the thermo-plastic problem within a time step Δt.

4. Numerical results and discussion

In this section, firstly, the proposed thermo-mechanical coupled microscale plasticity model and its numerical implementation are validated by comparisons with the experiment results and a benchmark numerical example. Then, the coupling effect of strain gradient strengthening and thermal softening on the microscale plastic behavior of metallic materials is investigated through the tensile behavior of the plate with a hole in its center.

4.1. Validation of the model and the numerical implementation

The verification process of the effectiveness of the thermo-mechanical coupled microscale plasticity model is divided into three parts: the verification of the effectiveness of the numerical implementation of the strain gradient plasticity model, the verification of the effectiveness of the numerical implementation of the thermal effect on plastic behavior, and the verification of the effectiveness of the numerical implementation of staggered solution scheme. It should be noted that we validated the effectiveness of the above three parts separately.

(1) The verification of the effectiveness of the numerical implementation of the strain gradient plasticity model: the bending test of Ni foils

When validating the effectiveness of the numerical implementation of the strain gradient plasticity model, the thermal effect is not considered. The bending of Ni foils is often used to validate the effectiveness of the phenomenological model by previous researchers (Chakravarthy and Curtin, 2011). Therefore, the bending test of Ni foils is used to verify the effectiveness of our model in the numerical implementation of the strain gradient plasticity model. Ehrler et al. (2008) measured the stress-strain relationship of Ni foils in flexure by the load-unload method, which provided accurate data from the elastic region to high plastic strain. The schematic of the load-unload method is shown in Fig. 3. The Ni films used in the bending test are obtained commercially.

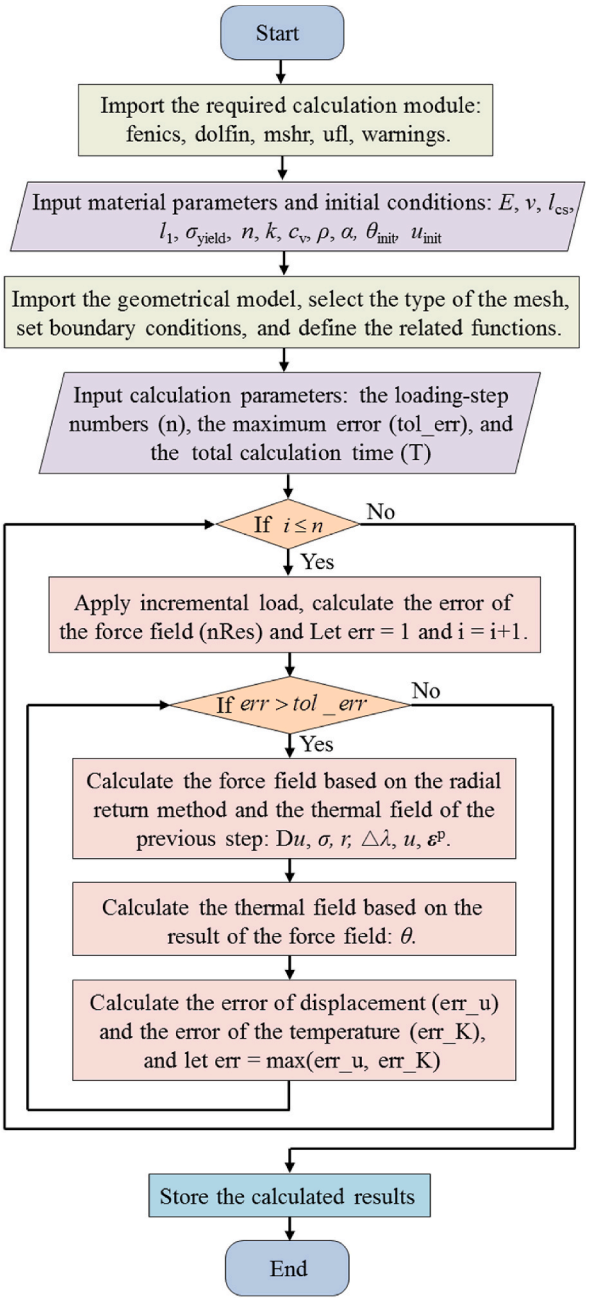

Fig. 2. The numerical implementation algorithm of the thermo-mechanical coupled lower-order strain gradient plasticity model.

The thicknesses h of the three specimens are 10 μm, 50 μm, and 125 μm of purity 99.95%, 99.90%, and 99.99%. The average grain size d is about 30 μm at each thickness. According to the experiment, the modulus of the Ni film is about 200 GPa, and the Poisson's ratio of the Ni foils is taken to be 0.31. The yield strength is calibrated by simulating the bending behavior of Ni with a thickness of 125 μm. By comparing the simulation results with the experiment, the yield strength is determined as 50 MPa. The power hardening exponent is taken to be 0.2 based on the previous study (Song and Voyiadjis, 2018). Referring to the previous study (Chen and Wang, 2000), the intrinsic characteristic length parameters of Ni foil for the rotation gradient and the stretch gradient are 3.3 μm and 3 μm, respectively.

The measurement results for Ni foils with different thicknesses and the corresponding numerical values based on our model are presented in Fig. 4. As shown in this figure, strong size-dependent plastic behaviors

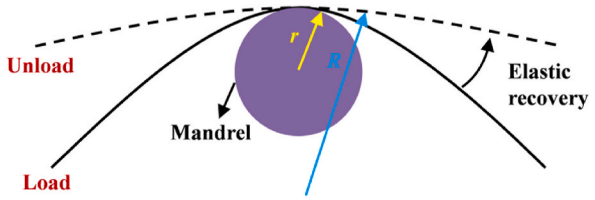

Fig. 3. The schematic of the load-unload method. The solid line represents the Ni foil in the loaded state, and the dashed line represents the Ni foil in the unloaded state after elastic recovery.

are observed in the relationship between the normalized bending stress and the surface strain. Under the same surface strain, the normalized bending stress increases with the decreasing thickness of Ni foils in the plastic stage. Namely, the yield path of metallic materials at the microscale strongly depends on the state of the strain gradient. The simulation results can reproduce the size-dependence phenomenon in the bending test of Ni films, which shows that the numerical implementation of the strain gradient plasticity in our code is effective. However, there are still some errors between the simulation and the experiment at the beginning stage where $h = 125$ μm and at the finishing stage where $h = 10$ μm. At the beginning stage where $h = 125$ μm, the slope of the simulation result is higher than that of the experiment, and the difference between them is about 32.2%. At the finishing stage where $h = 10$ μm, the simulation is lower than the experiment, and the difference between them is about 10%. The reasons for this are as follows. First, the size-dependence behavior in the elastic stage is not considered in the lower-order strain gradient plasticity. In the simulation, the modulus is set to be a constant (200 GPa), which leads to the error between the simulation and the experiment at the beginning stage where $h = 125$ μm. Second, our model is isotropic. However, in practice, the Ni film is not completely isotropic. The difference between the model and the reality leads to the error between the simulation results and the experiment.

(2) The verification of the effectiveness of the numerical implementation of the thermal effect on plastic behavior: the tensile behavior of Ni film

When validating the effectiveness of the numerical implementation of the thermal effect on plastic behavior, the strain gradient effect is not

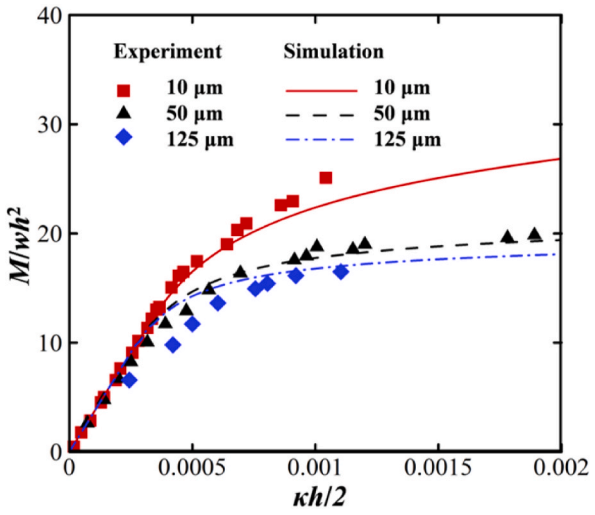

Fig. 4. The relationship between the normalized bending stress M/wh^2 and the surface strain $\kappa h/2$. W is the width of the Ni foils and κ is the curvature of the Ni foils in the loaded state. The symbols are for the experiments (Ehrler et al., 2008), and the lines are for the simulation results.

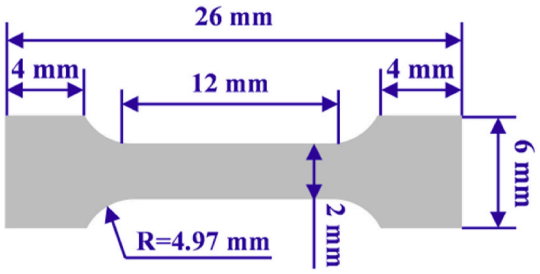

Fig. 5. The schematic of the dog bone specimen and its dimensions (Seungwoo et al., 2008).

considered. Seungwoo et al. (2008) developed a micro tensile testing system that consists of a high-temperature furnace and a digital image correlation system to investigate the tensile behavior of Ni film at high temperatures. The Ni films used in the tensile test were prepared by MEMS processes and electroplating. The schematic of the dumbbell-shaped specimen used in the experiment is shown in Fig. 5. Referring to the work of Seungwoo et al. (2008), the modulus and Poisson's ratio of Ni film are 115 GPa and 0.31, respectively. The power hardening exponent is taken to be 0.2. The yield strength is calibrated by simulating the tensile behavior of Ni at different temperatures, and then the relationship between the yield strength and the temperature is fitted. Combining the simulation results and the experiment, it can be found that the linear function ($\sigma_{y_0} = \sigma_{y_0}^{\theta=0} - k_\theta \cdot \theta$) can fit the relation between the yield strength and the temperature well. The yield strength $\sigma_{y_0}^{\theta=0}$ and k_θ are respectively calibrated as 400 MPa and 0.778 MPa $^\circ C^{-1}$ based on the experiment data. Referring to the previous study (Song and Voyiadjis, 2018), the density, specific heat capacity, thermal diffusion coefficient, and thermal expansion coefficient of the Ni film are taken as 8.902 g/cm^3, 0.54 (J/g)·K, 2.042·10^{-5} m^2/J and 13.1 (μm/m)·K, respectively.

Fig. 6 displays the comparisons between the simulation results calculated by our model and the experiment results at four different temperatures, i.e. 18 °C, 75 °C, 145 °C, and 218 °C. From this figure, it can be found that the temperature-dependent plastic behavior is presented in the stress-strain relationship. The initial yield strength decreases with the increase in temperature, and the yield path is almost parallel to each other at different temperatures. In other words, the temperature significantly influences the initial yield strength but has no effect on the yield path. In addition, the temperature has little effect on

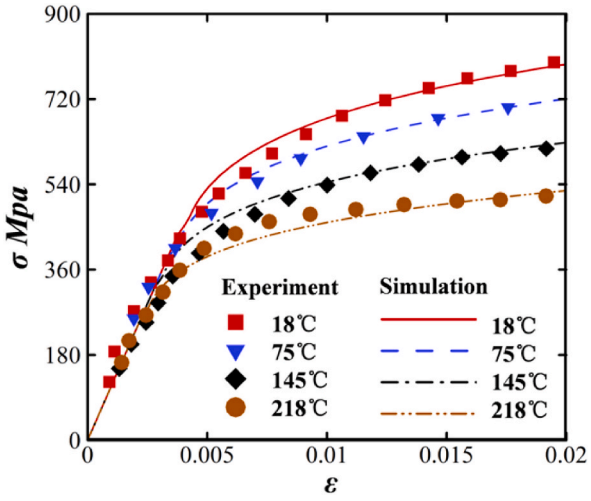

Fig. 6. The stress-strain response of Ni film at four different temperatures. The symbols are for the experiments (Seungwoo et al., 2008), and the lines are for the simulation results calculated by our model.

the modulus of Ni films. What needs to be emphasized is that the simulation results calculated by our model and the experiment data correspond closely with each other, which implies that the numerical implementation of the thermal effect on plastic behavior in our code is effective.

(3) The verification of the effectiveness of the numerical implementation of the staggered solution scheme: the thermo-plastic coupled problem of cylinder expansion

When validating the effectiveness of the numerical implementation of the staggered solution scheme, the strain gradient effect is not considered. As a commercial code, ABAQUS has good performance in solving the thermo-plastic coupling problem. Therefore, the simulation results of ABAQUS are considered as benchmarks to verify the effectiveness of our code in the numerical implementation of the staggered solution scheme. The model used in ABAQUS is the same as that used in our code. The schematic of the cylinder expansion problem including the physical model, boundary conditions, and initial conditions is shown in Fig. 7. The material parameters for the physical model are determined with reference to those of Al. The modulus, yield strength, and Poisson's ratio are 70 GPa, 250 MPa, and 0.3, respectively. In the plastic stage, the linear hardening mode is adopted, and the hardening modulus is set to 707.07 MPa. The density, specific heat capacity, thermal diffusion coefficient, and thermal expansion coefficient are taken as 2.7 g/cm^3, 0.88 (J/g)·K, 2.5·10^{-4} m^2/J and 10 (μm/m)·K, respectively.

The distributions of the total displacement, effective plastic strain, and temperature calculated by ABAQUS and our code are shown in Fig. 8. As shown in this figure, we can find that the calculation results of our code are consistent with those of ABAQUS. To quantify the error between the calculation results of ABAQUS and those of our code, the results on the A-B line are shown in Fig. 9. As we can see, the maximum differences between the results of ABAQUS and those of our code in the displacement magnitude, the effective plastic strain and the temperature are less than 1%. It can be seen from the comparisons that the numerical implementation of the staggered solution scheme in our code is effective. In addition, the CPU time used by our code is longer than that by ABAQUS. In future work, we will further improve the computational efficiency of our code.

4.2. *Coupling effect of strain gradient strengthening and thermal softening*

Based on the results of Section 4.1, it can be known that the proposed thermo-mechanical coupled microscale plasticity model and its numerical implementation are effective. In this section, taking the tensile of a plate with a hole in its center as an example, the coupling effect of strain gradient strengthening and thermal softening on the plastic behavior of metallic materials is investigated by numerical simulations. In order to

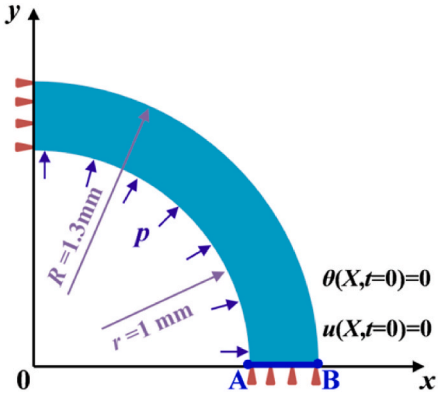

Fig. 7. The schematic of the cylinder expansion problem including the physical model, the boundary conditions, and the initial conditions.

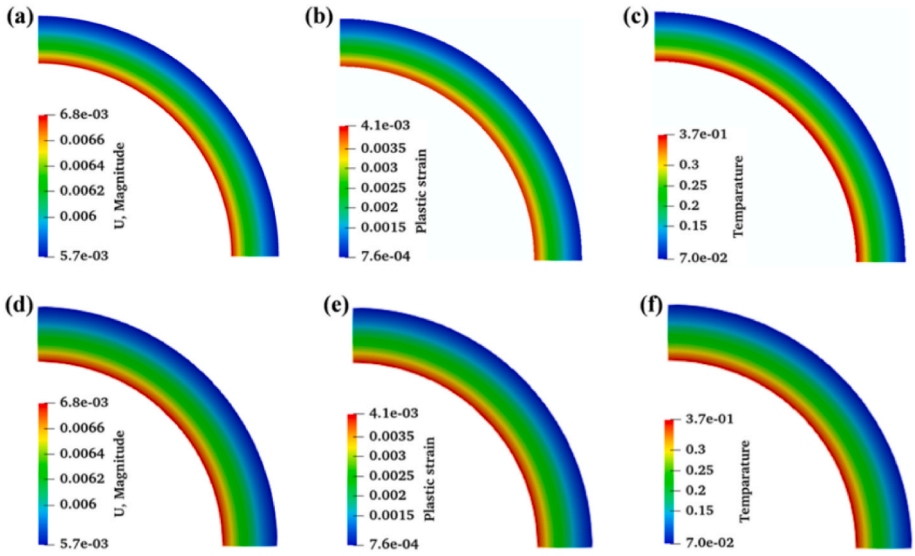

Fig. 8. The comparison between the calculation results of ABAQUS and those of our code. (a) and (d) are the distributions of the total displacement; (b) and (e) are the distributions of the effective plastic strain; (c) and (f) are the distributions of the temperature. (a), (b) and (c) are the results of ABAQUS. (d), (e) and (f) are the results of our code.

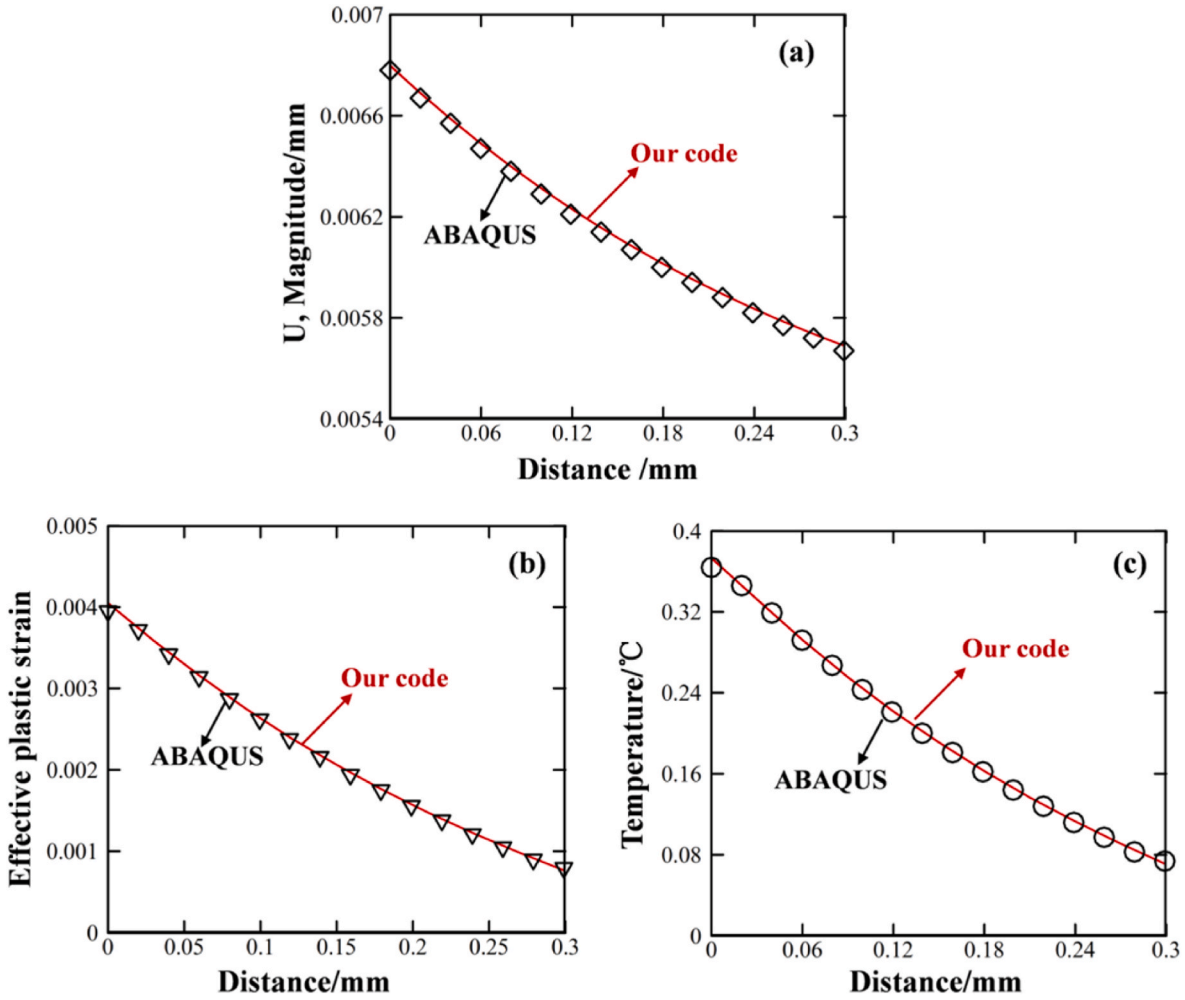

Fig. 9. The comparisons between the calculation results of ABAQUS and those of our code on the A-B line. (a) The magnitude of displacement; (b) Effective plastic strain; (c) Temperature.

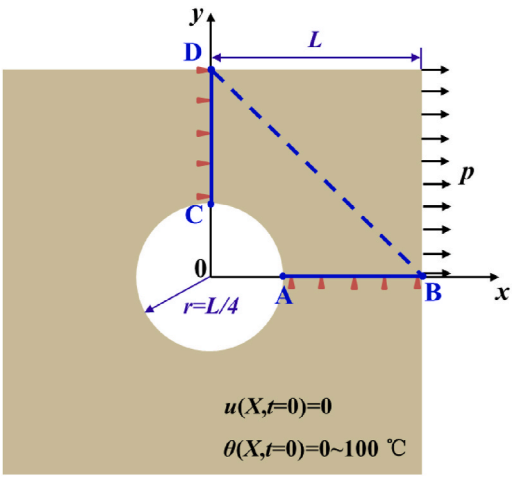

Fig. 10. The tensile schematic of a plate with a hole in its center including the main dimension, boundary conditions, and initial conditions.

better understand the effects of strain gradient and temperature on the plastic behavior of metallic materials, a two-step method is adopted. Firstly, only the influence of strain gradient on the plastic behavior including the hardening response and the heat generation is studied. Secondly, the coupling effect of strain gradient and temperature is investigated.

The schematic of this tensile problem is shown in Fig. 10. Because this tensile problem is symmetric about the x and y axes, in order to reduce the calculation cost, a quarter of the plate is used for the simulation. The material parameters used in the simulation are introduced as follows. Referring to the mechanical properties of Al, the modulus and Poisson's ratio are taken to be 70 GPa and 0.3, respectively. In the plastic stage, the power law hardening mode is adopted, and the power hardening exponent is set to 0.2. Referring to the previous study (Aldakheel and Miehe, 2017), the ratio of the intrinsic characteristic length parameter l to the width of the model L is from 0 to 0.1. The yield strength $\sigma_{y_0}^{\theta=0}$ and k_θ are set to 250 MPa and 0.8 MPa $^\circ C^{-1}$, respectively. Referring to the thermal properties of Ni, the density, specific heat capacity, thermal diffusion coefficient, and thermal expansion coefficient are taken as 8.902 g/cm^3, 0.54 (J/g)·K, 2.042·10^{-5} m^2/J and 13.1 (μm/m)·K, respectively. The initial displacement $\boldsymbol{u}(\boldsymbol{X}, t=0)$ is 0, and the initial temperature $\theta(\boldsymbol{X}, t=0)$ is from 0 to 100 °C. There is no heat conduction between the plate and the surrounding environment.

(1) Influence of strain gradient on the plastic hardening and heat generation

When the influence of strain gradient on the plastic behavior is studied, the initial temperature $\theta(\boldsymbol{X}, t=0)$ is set to be 0 °C. Fig. 11

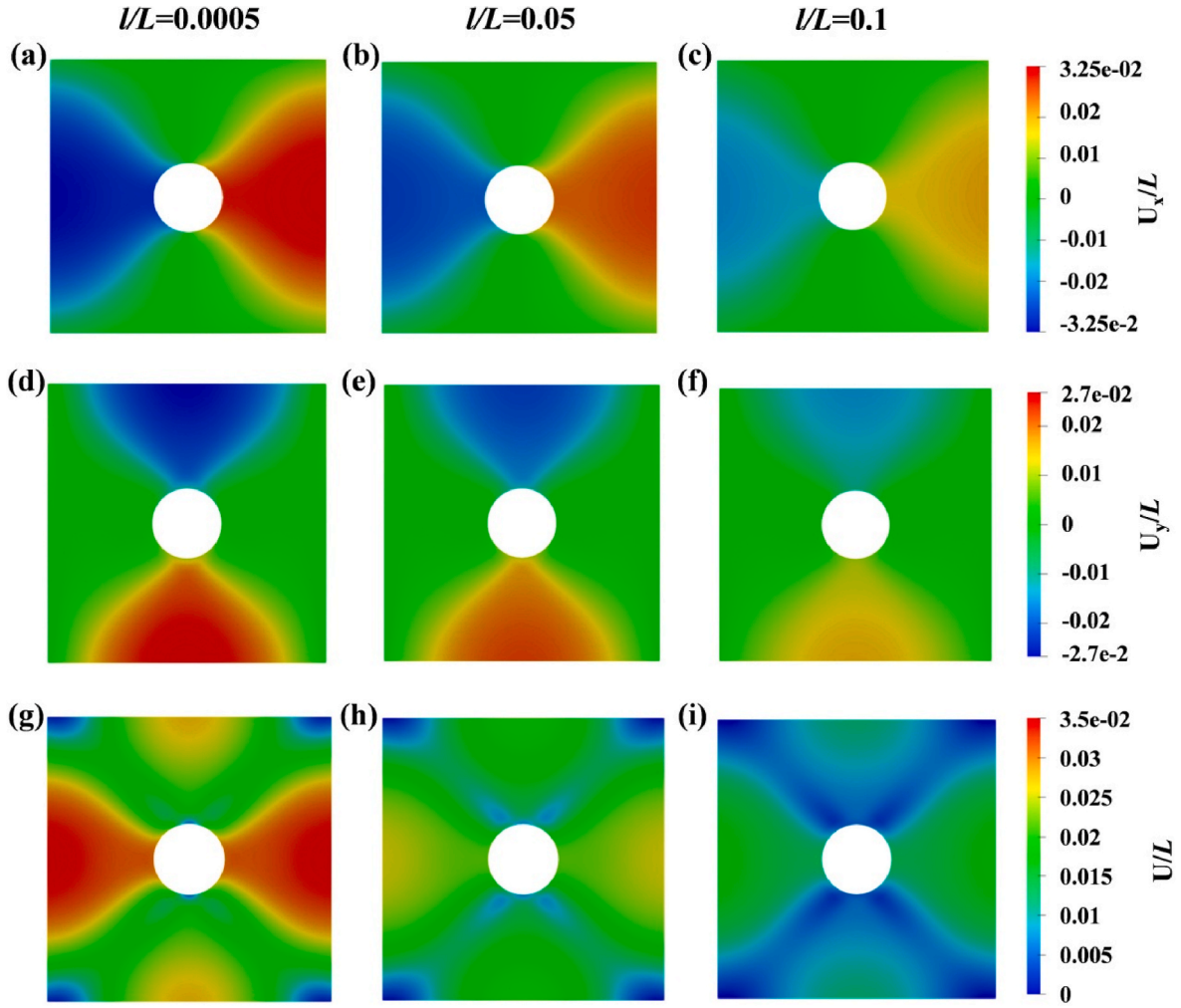

Fig. 11. The distribution of the displacement at the final deformation with $\theta(X, t=0)=0$. Distributions of displacement in x (a)–(c), displacement in y (d)–(f), and displacement magnitude (g)–(i) for three different characteristic length scales: $l/L=0.0005$ in (a), (d), and (g); $l/L=0.05$ in (b), (e) and (h); $l/L=0.1$ in (c), (f) and (i).

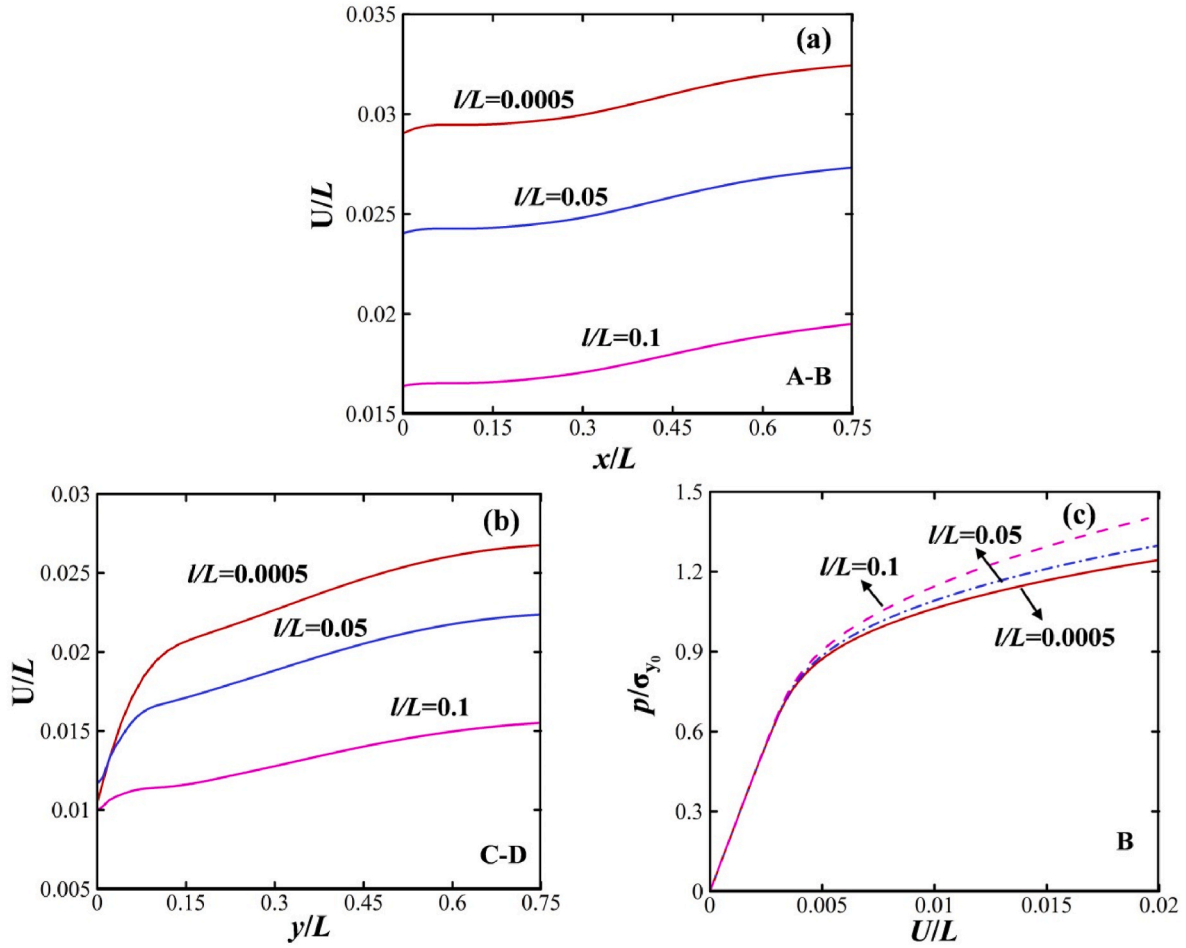

Fig. 12. The distributions of the displacement magnitude on the A-B line (a) and the C-D line (b) at the final deformation, and the load-displacement relationship at point B (c).

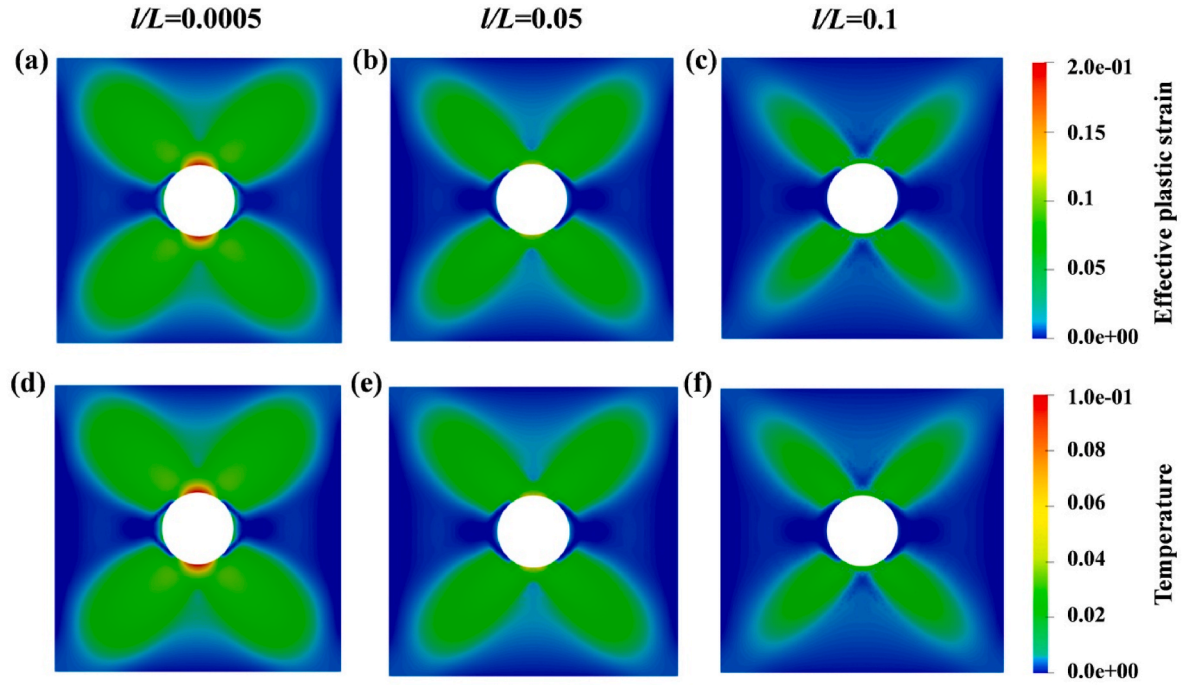

Fig. 13. Distributions of effective plastic strain (a)–(c), and temperature (d)–(f) at the final deformation for three different characteristic length scales with $\theta(X, t = 0) = 0$: $l/L = 0.0005$ in (a) and (d); $l/L = 0.05$ in (b) and (e); $l/L = 0.1$ in (c) and (f).

depicts the distributions of displacement at the final deformation for three different ratios of the characteristic length parameter l to the width of model L. From this figure, it can be observed that the strain gradient significantly affects structural deformations. For example, the displacement decreases with the increase of l/L. In order to understand the enhancement effect of strain gradient more intuitively, the distributions of U/L on A-B and C-D lines at different l/L are presented in Fig. 12 (a) and (b). As we can see from the figure, the larger the l/L, the smaller the U/L at the same position. The reason for this is that the closer the intrinsic characteristic length parameter is to the structure size, the more obvious the enhancement effect of the strain gradient on the plastic hardening, which is shown in Fig. 12(c). It can be known that the larger the l/L, the smaller the U/L under the same load p/σ_{y0}. Namely, the strain gradient effect enhances the mechanical behavior of the structure, which lays a foundation for the understanding of the coupling effect of strain gradient and temperature.

The strain gradient also significantly influences the distributions of effective plastic strain and temperature. Fig. 13 presents the distributions of effective plastic strain and temperature at the final deformation for three different ratios of the characteristic length l to the width of the plate L. From this figure, it can be observed that a concentration of the effective plastic strain in Fig. 13(c) and the temperature in Fig. 13(f) in the diagonal direction for $l/L = 0.1$. When l/L decreases, the effective plastic strain and the temperature spread out. To see it more intuitively, the distributions of effective plastic strain and temperature on the B-D line are shown in Fig. 14. From this figure, it can be seen that the height and the width of the distribution of effective plastic strain and temperature on the B-D line decrease with the increase of l/L. The above phenomenon shows that the strengthening effect of the strain gradient inhibits the development of plastic deformations, which further affects the heat generation in the stage of plastic deformations.

(2) Coupling effect of strain gradient and temperature on the plastic behavior

In order to investigate the coupling effect of strain gradient and temperature, the tensile behaviors of the plate at two different ratios of the characteristic length l to the width of the model L and three different temperatures are simulated. The distributions of displacement and effective plastic strain at three different temperatures with $l/L = 0$ and $l/L = 0.05$ are shown in Fig. 15. From this figure, we can see that the higher the temperature, the larger the displacement, and the wider the plastic zone. Namely, the increase in temperature weakens the mechanical behaviors of metallic materials. In addition, it can be observed that the displacement and the plastic zone decrease at the same temperature when l/L changes from 0 to 0.05, which implies that the strain gradient enhances the mechanical properties of metallic materials. To quantitatively show the coupling effect of strain gradient and temperature on the plastic deformation of metallic materials, U/L on the A-B and C-D lines and the effective plastic strain on the B-D line are shown in Fig. 16 (a), (b), and (c). These figures show that when the strain gradient effect is neglected, the displacement at the same position increases with the increase in temperature, and so do the height and width of the distribution of effective plastic strain on the B-D line. The reason for this is that the yield strength decreases with the increase in temperature. When the strain gradient effect is further considered on the basis of considering the thermal effect, the displacement at the same position and the height and width of the distribution of effective plastic strain will decrease. For example, U/L of the point B increases from 0.0075 to 0.0265 when the temperature changes from 0 to 100 °C for the case where l/L equals 0, and decreases from 0.02653 to 0.0205 when l/L changes from 0 to 0.05 for the case where the temperature is 100 °C. The above phenomenon shows that the plastic behavior of microscale metallic materials at high temperatures depends on the competition between thermal softening and strain gradient strengthening. The same phenomenon also can be found in the load-displacement relationship at point B as shown in Fig. 16 (d). From this figure, it can be observed that when only the thermal effect is considered, the higher the temperature, the lower the load in the plastic stage. In addition, the yield paths at different temperatures do not intersect each other, which implies that the temperature has no effect on the evolution path of plastic deformations. This phenomenon is also found in previous experimental studies (Wheeler et al., 2013). When the strain gradient effect is further considered on the basis of the consideration of the thermal effect, the load in the plastic stage will be larger than the case where the strain gradient effect is neglected, and the path of the plastic deformation will not be parallel to that at zero temperature.

5. Conclusions and future work

In order to describe the deformation behavior of microscale metallic materials at high temperatures, the thermal effect is incorporated into the C–W theory to establish a new thermo-mechanical coupled microscale plasticity model and a finite element solution algorithm for this model is proposed. Taking the tensile behavior of a plate with a hole in its center as an example, the coupling effect of strain gradient strengthening and thermal softening on the plastic behavior of metallic materials is investigated based on our model. The main conclusions are as follows:

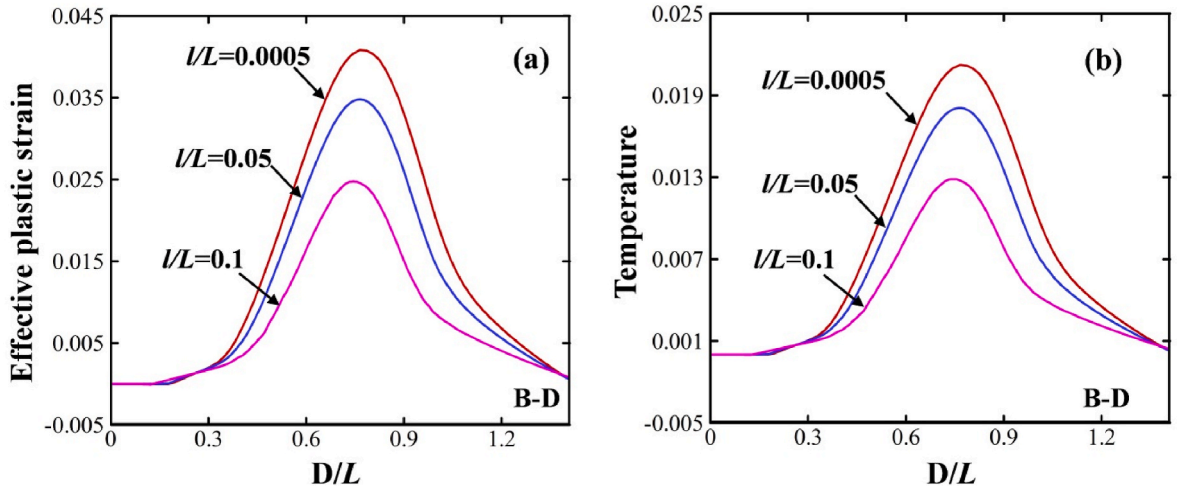

Fig. 14. The distributions of effective plastic strain and temperature on the B-D line.

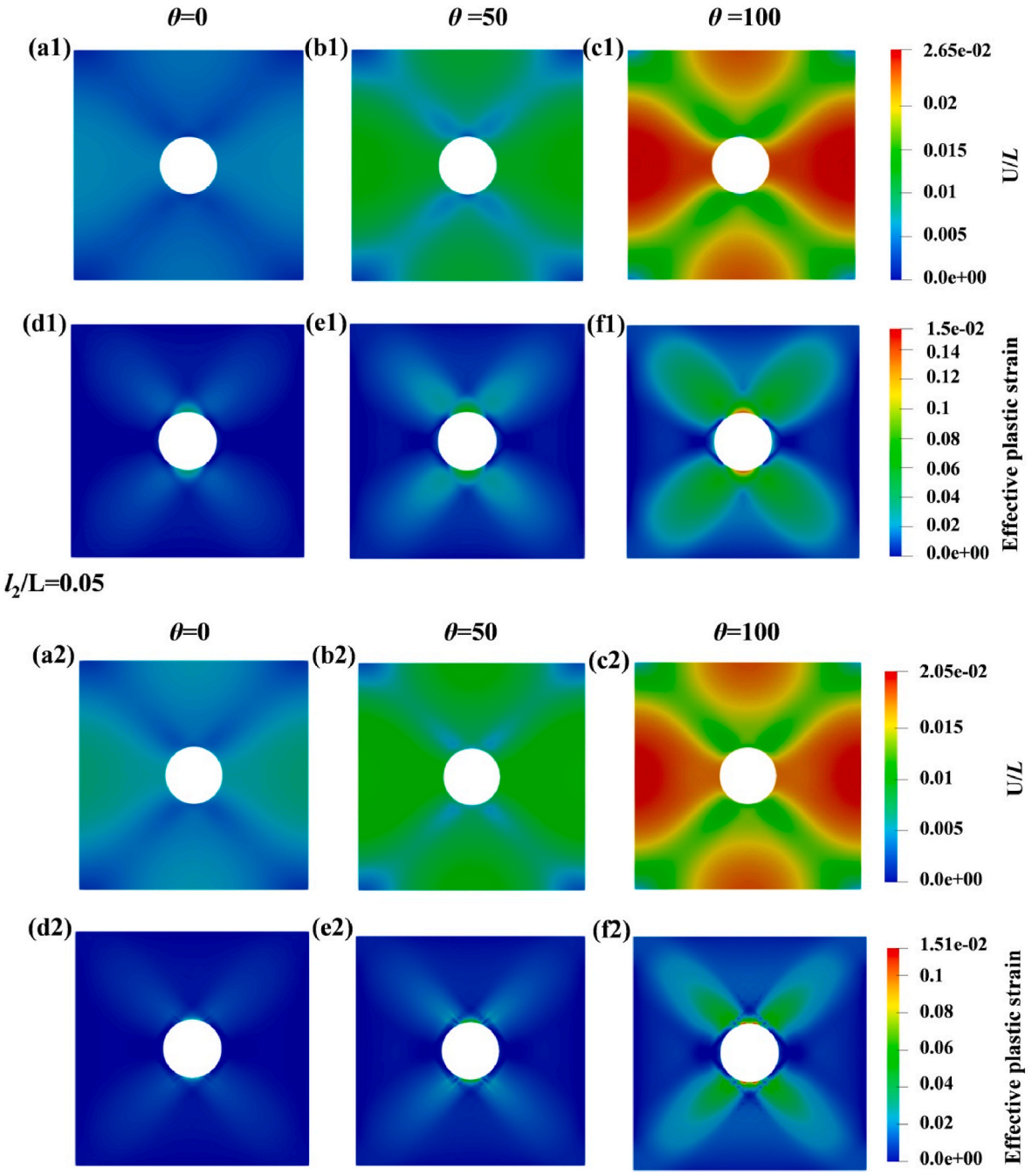

Fig. 15. Distributions of displacement magnitude (a)–(c), and effective plastic strain (d)–(f) at the final deformation for three different initial temperatures: (a) and (d) $\theta = 0$; (b) and (e) $\theta = 50$ and $\theta = 100$ in (c) and (f). "1" is for the case where l/L $= 0$, and "2" is for the case where $l/L = 0.05$.

(1) By comparisons with previous experimental results and a benchmark numerical example, our model has proved to be effective in simulating the microscale plastic behavior of metallic materials under different temperatures. In addition, the finite element algorithm combining the radial return method and the staggered solution scheme is proved to be a good numerical implementation solution to the thermal-mechanical coupled microscale plasticity model.

(2) The closer the material size is to the characteristic length parameter, the more obvious the strain gradient effect is. The strain gradient effect will strengthen the mechanical behavior of the structure, restrain the development of the plastic zone, and reduce heat generation in the stage of plastic deformations.

(3) The plastic behavior of microscale metallic materials at high temperatures depends on the competition between thermal softening and strain gradient strengthening.

The current work mainly investigates the small deformation plastic behavior of microscale metallic materials at high temperatures under the framework of lower-order strain gradient plasticity. The model we proposed is preliminarily verified by experiments. It should be emphasized that full thermomechanical experiments are still needed to further verify our model, which will be one of the most important future directions. When the deformation is not infinitesimal, the thermomechanical coupled strain gradient plasticity for the finite deformation should be used. In addition, the fracture is not considered in our current model, while in future work the cohesive zone model or phase-

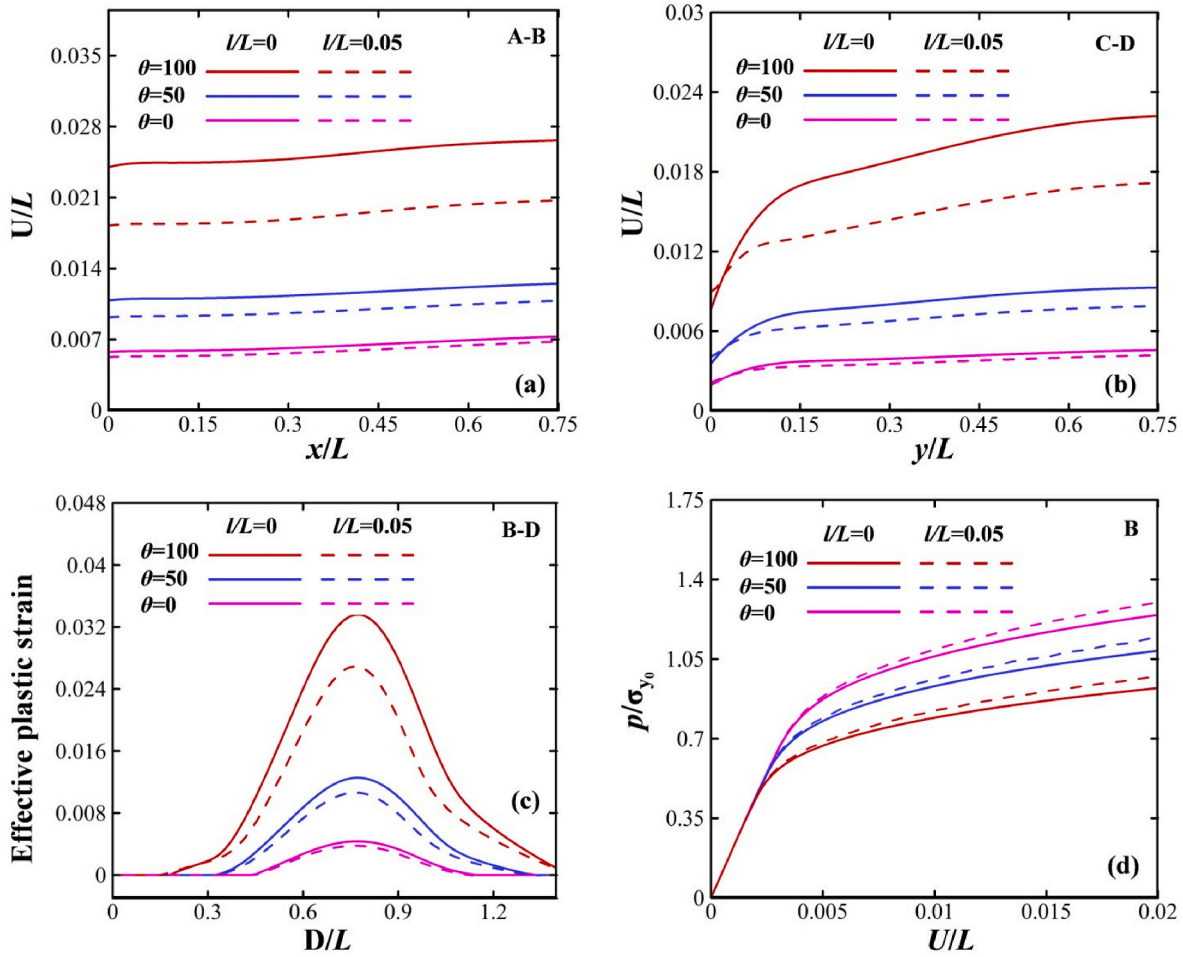

Fig. 16. The distributions of U/L on the A-B line (a) and on the C-D line (b), and the effective plastic strain (c) on the B-D line at the final deformation for three different initial temperatures with l/L equals 0 and 0.05. (d) is the load-displacement relationship at point B.

field fracture model can be incorporated into the model to study the fracture behavior of metallic materials under the coupling effect of thermal softening and strain gradient strengthening. The method in this work can also be used to construct the lower-order strain gradient plasticity theory coupled with other physical fields, which provides an opportunity to study the microscale mechanical behavior of metallic materials under multi-field coupling.

Credit author statement

Yanwei Liu: Conceptualization, Formal analysis, Methodology, Funding acquisition, Resources, Writing - original draft. Hao Long: Methodology, Formal analysis, Writing - review & editing. Siyuan Zhang: Methodology, Formal analysis, Writing - review & editing. Qianqian Zhou: Methodology, Writing - review & editing. Jingru Song: Methodology, Writing - review & editing. Yueguang Wei: Conceptualization, Funding acquisition, Resources, Writing - review & editing.

Declaration of competing interest

The authors declare that they have no known competing financial interests or personal relationships that could have appeared to influence the work reported in this paper.

Data availability

Data will be made available on request.

Acknowledgment

This work was supported by the Postdoctoral Science Foundation of China for Innovative Talents (Grant nos. BX20220008) and the National Natural Science Foundation of China (Grant nos. 11890681, 12032001, 11521202, and 12202007).

Appendix. The derivation of the balance equation of the thermal field in the traditional case

In the traditional case, Helmholtz's free energy ψ is considered as a function of temperature θ, total strain $\boldsymbol{\varepsilon}$, plastic strain $\boldsymbol{\varepsilon}^p$, and cumulative effective plastic strain $\bar{\varepsilon}^p$:

$$\psi = \psi(\theta, \boldsymbol{\varepsilon} - \boldsymbol{\varepsilon}^p, \bar{\varepsilon}^p) \tag{A1}$$

Based on Eq. (A1), $\dot{\psi}$ can be expressed as

$$\dot{\Psi} = -s\dot{\theta} + \frac{\partial \Psi}{\partial(\boldsymbol{\varepsilon} - \boldsymbol{\varepsilon}^p)} : \left(\dot{\boldsymbol{\varepsilon}} - \dot{\boldsymbol{\varepsilon}}^p\right) + \frac{\partial \Psi}{\partial \bar{\varepsilon}^p}\dot{\bar{\varepsilon}}^p \tag{A2}$$

With the relationship $s = -\frac{\partial \Psi}{\partial \theta}$ in mind, then $\dot{s}$ can be obtained:

$$\dot{s} = -\frac{\partial^2 \Psi}{\partial \theta^2}\dot{\theta} - \frac{\partial^2 \Psi}{\partial(\boldsymbol{\varepsilon} - \boldsymbol{\varepsilon}^p)\partial\theta} : \dot{\boldsymbol{\varepsilon}} + \frac{\partial^2 \Psi}{\partial(\boldsymbol{\varepsilon} - \boldsymbol{\varepsilon}^p)\partial\theta} : \dot{\boldsymbol{\varepsilon}}^p - \frac{\partial^2 \Psi}{\partial \bar{\varepsilon}^p \partial\theta}\dot{\bar{\varepsilon}}^p \tag{A3}$$

Combining Eq (9), (A2), and (A3), one can get

$$\begin{aligned} &-\rho\theta \frac{\partial^2 \Psi}{\partial(\boldsymbol{\varepsilon} - \boldsymbol{\varepsilon}^p)\partial\theta} : \dot{\boldsymbol{\varepsilon}} + \rho\left(\theta \frac{\partial^2 \Psi}{\partial(\boldsymbol{\varepsilon} - \boldsymbol{\varepsilon}^p)\partial\theta} - \frac{\partial \Psi}{\partial(\boldsymbol{\varepsilon} - \boldsymbol{\varepsilon}^p)}\right) : \cdot\, \boldsymbol{\varepsilon}^p + \left(\rho \frac{\partial \Psi}{\partial(\boldsymbol{\varepsilon} - \boldsymbol{\varepsilon}^p)} - \boldsymbol{\sigma}\right) : \dot{\boldsymbol{\varepsilon}} \\ &+\rho\left(\frac{\partial \Psi}{\partial \bar{\varepsilon}^p} - \theta \frac{\partial^2 \Psi}{\partial \bar{\varepsilon}^p \partial\theta}\right) \cdot\, \bar{\varepsilon}^p - \rho\theta \frac{\partial^2 \Psi}{\partial \theta^2}\dot{\theta} = r - \nabla \cdot \boldsymbol{q} \end{aligned} \tag{A4}$$

According to the definition of specific heat capacity $c_\varepsilon = -\theta \partial^2 \Psi / \partial \theta^2$, Eq. (A4) can be expressed as

$$\begin{aligned} \rho c_\varepsilon \dot{\theta} = k\nabla^2\theta + r + \rho\theta \frac{\partial^2 \Psi}{\partial(\boldsymbol{\varepsilon} - \boldsymbol{\varepsilon}^p)\partial\theta} : \left(\dot{\boldsymbol{\varepsilon}} - \dot{\boldsymbol{\varepsilon}}^p\right) + \rho \frac{\partial \Psi}{\partial(\boldsymbol{\varepsilon} - \boldsymbol{\varepsilon}^p)} : \dot{\boldsymbol{\varepsilon}}^p \\ + \left(\rho \frac{\partial \Psi}{\partial(\boldsymbol{\varepsilon} - \boldsymbol{\varepsilon}^p)} - \boldsymbol{\sigma}\right) : \dot{\boldsymbol{\varepsilon}} - \rho\left(\frac{\partial \Psi}{\partial \bar{\varepsilon}^p} - \theta \frac{\partial^2 \Psi}{\partial \bar{\varepsilon}^p \partial\theta}\right)\dot{\bar{\varepsilon}}^p \end{aligned} \tag{A5}$$

To simplify Eq. (14), we need to know the specific expression of Ψ. According to the second-order Taylor expansion of Helmholtz free energy and the first law of thermodynamics, Ψ can be expressed as (Ottosen and Ristinmaa, 2005)

$$\rho\psi = \rho c_\varepsilon \left(\theta - \theta \ln \frac{\theta}{\theta^*}\right) + \frac{1}{2}(\boldsymbol{\varepsilon} - \boldsymbol{\varepsilon}^p) : \boldsymbol{D} : (\boldsymbol{\varepsilon} - \boldsymbol{\varepsilon}^p) - \boldsymbol{D} : \alpha I(\theta - \theta_0) : (\boldsymbol{\varepsilon} - \boldsymbol{\varepsilon}^p) + \rho\psi^p(\bar{\varepsilon}^p) \tag{A6}$$

where $\boldsymbol{D}$ is the fourth-order elastic tensor. It is noted that the coupling term of temperature and cumulative effective plastic strain is ignored. In addition, the constitutive equations can be obtained based on the thermodynamic low:

$$\boldsymbol{\sigma} = \rho \frac{\partial \psi}{\partial(\boldsymbol{\varepsilon} - \boldsymbol{\varepsilon}^p)}, s = -\frac{\partial \psi}{\partial \theta}, K = \rho \frac{\partial \psi}{\partial \bar{\varepsilon}^p} \tag{A7}$$

where K is the thermodynamic force that is energy conjugated to $\bar{\varepsilon}^p$. Using Eqs. (A6) and (A7) in Eq. (A5), the balance equation of the thermal field can be written as

$$\rho c_\varepsilon \dot{\theta} = k\nabla^2\theta + r - \theta \boldsymbol{D} : \alpha I : \left(\dot{\boldsymbol{\varepsilon}} - \dot{\boldsymbol{\varepsilon}}^p\right) + \boldsymbol{\sigma} : \dot{\boldsymbol{\varepsilon}}^p - K\dot{\bar{\varepsilon}}^p \tag{A8}$$

It is noted that ψ can also be considered as a function of temperature θ, elastic strain $\boldsymbol{\varepsilon}^e$, and cumulative effective plastic strain $\bar{\varepsilon}^p$: $\psi = \psi(\theta, \boldsymbol{\varepsilon}^e, \bar{\varepsilon}^p)$. At this time, the expression of Helmholtz's free energy is

$$\rho\psi = \rho c_\varepsilon \left(\theta - \theta \ln \frac{\theta}{\theta^*}\right) - \frac{1}{2}\alpha(\theta - \theta_0)\boldsymbol{I} : \boldsymbol{D} : \alpha(\theta - \theta_0)\boldsymbol{I} + \frac{1}{2}\boldsymbol{\varepsilon}^e : D : \boldsymbol{\varepsilon}^e + \rho\psi^p(\bar{\varepsilon}^p) \tag{A9}$$

Both Helmholtz's free energy expressions can derive the same equation.

References

Acharya, A., Bassani, J.L., 2000. Lattice incompatibility and a gradient theory of crystal plasticity. J. Mech. Phys. Solid. 48, 1565–1595.

Acharya, A., Beaudoin, A., 2000. Grain-size effect in viscoplastic polycrystals at moderate strains. J. Mech. Phys. Solid. 48, 2213–2230.

Acharya, A., Shawki, T., 1995. Thermodynamic restrictions on constitutive equations for second-deformation-gradient inelastic behavior. J. Mech. Phys. Solid. 43, 1751–1772.

Acharya, A., Tang, H., Saigal, S., Bassani, J.L., 2004. On boundary conditions and plastic strain-gradient discontinuity in lower-order gradient plasticity. J. Mech. Phys. Solid. 52, 1793–1826.

Aldakheel, F., Miehe, C., 2017. Coupled thermomechanical response of gradient plasticity. Int. J. Plast. 91, 1–24.

Alnæs, M., Blechta, J., Hake, J., Johansson, A., Kehlet, B., Logg, A., Richardson, C., Ring, J., Rognes, M.E., Wells, G.N., 2015. The FEniCS project version 1.5. Archive of Numerical Software 3.

Anand, L., Aslan, O., Chester, S.A., 2012. A large-deformation gradient theory for elastic-plastic materials: strain softening and regularization of shear bands. Int. J. Plast. 30–31, 116–143.

Arora, A., Arora, R., Acharya, A., 2023. Interface-dominated plasticity and kink bands in metallic nanolaminates. Crystals 13, 828.

Askari, H., Maughan, M.R., Abdolrahim, N., Sagapuram, D., Bahr, D.F., Zbib, H.M., 2015. A stochastic crystal plasticity framework for deformation of micro-scale polycrystalline materials. Int. J. Plast. 68, 21–33.

Ban, H., Yao, Y., Chen, S., Fang, D., 2017. The coupling effect of size and damage in micro-scale metallic materials. Int. J. Plast. 95, 251–263.

Beaudoin, A.J., Acharya, A., Chen, S., Korzekwa, D., Stout, M., 2000. Consideration of grain-size effect and kinetics in the plastic deformation of metal polycrystals. Acta Mater. 48, 3409–3423.

Bertram, A., Forest, S., 2014. The thermodynamics of gradient elastoplasticity. Continuum Mech. Therm. 26, 269–286.

Bittencourt, E., 2018. On the effects of hardening models and lattice rotations in strain gradient crystal plasticity simulations. Int. J. Plast. 108, 169–185.

Chakravarthy, S.S., Curtin, W., 2011. Stress-gradient plasticity. Proc. Natl. Acad. Sci. USA 108, 15716–15720.

Chen, L., Edwards, T.E.J., Di Gioacchino, F., Clegg, W.J., Dunne, F.P., Pham, M.-S., 2019. Crystal plasticity analysis of deformation anisotropy of lamellar TiAl alloy: 3D microstructure-based modelling and in-situ micro-compression. Int. J. Plast. 119, 344–360.

Chen, S., Wang, T., 2000. A new hardening law for strain gradient plasticity. Acta Mater. 48, 3997–4005.

Chen, S., Wang, T., 2001. Strain gradient theory with couple stress for crystalline solids. Eur. J. Mech. Solid. 20, 739–756.

Danas, K., Deshpande, V.S., Fleck, N., 2012. Size effects in the conical indentation of an elasto-plastic solid. J. Mech. Phys. Solid. 60, 1605–1625.

Demiral, M., Roy, A., El Sayed, T., Silberschmidt, V.V., 2014. Influence of strain gradients on lattice rotation in nano-indentation experiments: a numerical study. Mater. Sci. Eng., A 608, 73–81.

Dunstan, D., Bushby, A., 2013. The scaling exponent in the size effect of small scale plastic deformation. Int. J. Plast. 40, 152–162.

Ehrler, B., Hou, X., Zhu, T., P'ng, K.M., Walker, C.J., Bushby, A., Dunstan, D.J., 2008. Grain size and sample size interact to determine strength in a soft metal. Phil. Mag. 88, 3043–3050.
Faghihi, D., Voyiadjis, G.Z., 2014. A thermodynamic consistent model for coupled strain-gradient plasticity with temperature. J. Eng. Mater. Technol. 136.
Farokhi, H., Ghayesh, M.H., 2017. Nonlinear thermo-mechanical behaviour of MEMS resonators. Microsyst. Technol. 23, 5303–5315.
Fleck, N., Hutchinson, J., Willis, J., 2014. Strain gradient plasticity under non-proportional loading. Proc. R. Soc. A 470, 20140267.
Fleck, N., Hutchinson, J., Willis, J., 2015. Guidelines for constructing strain gradient plasticity theories. J. Appl. Mech. 82.
Fleck, N.A., Hutchinson, J.W., 2001. A reformulation of strain gradient plasticity. J. Mech. Phys. Solid. 49, 2245–2271.
Fleck, N.A., Willis, J.R., 2009. A mathematical basis for strain-gradient plasticity theory-Part I: scalar plastic multiplier. J. Mech. Phys. Solid. 57, 161–177.
Forest, S., Aifantis, E.C., 2010. Some links between recent gradient thermo-elasto-plasticity theories and the thermomechanics of generalized continua. Int. J. Solid Struct. 47, 3367–3376.
Galetto, M., Schiavi, A., Genta, G., Prato, A., Mazzoleni, F., 2019. Uncertainty evaluation in calibration of low-cost digital MEMS accelerometers for advanced manufacturing applications. CIRP Annals 68, 535–538.
Gao, H., Huang, Y., Nix, W., Hutchinson, J., 1999. Mechanism-based strain gradient plasticity—I. Theory. Journal of the Mechanics and Physics of Solids 47, 1239–1263.
Gudmundson, P., 2004. A unified treatment of strain gradient plasticity. J. Mech. Phys. Solid. 52, 1379–1406.
Gurtin, M.E., Anand, L., 2009. Thermodynamics applied to gradient theories involving the accumulated plastic strain: the theories of Aifantis and Fleck and Hutchinson and their generalization. J. Mech. Phys. Solid. 57, 405–421.
Gurtin, M.E., Reddy, B.D., 2014. Gradient single-crystal plasticity within a Mises–Hill framework based on a new formulation of self-and latent-hardening. J. Mech. Phys. Solid. 68, 134–160.
Haouala, S., Lucarini, S., Llorca, J., Segurado, J., 2020. Simulation of the Hall-Petch effect in FCC polycrystals by means of strain gradient crystal plasticity and FFT homogenization. J. Mech. Phys. Solid. 134, 103755.
Huang, Y., Qu, S., Hwang, K., Li, M., Gao, H., 2004. A conventional theory of mechanism-based strain gradient plasticity. Int. J. Plast. 20, 753–782.
Hutchinson, J.W., 2012. Generalizing J 2 flow theory: fundamental issues in strain gradient plasticity. Acta Mech. Sin. 28, 1078–1086.
Javed, Y., Mansoor, M., Shah, I.A., 2019. A review of principles of MEMS pressure sensing with its aerospace applications. Sens. Rev. 39, 652–664.
Jebahi, M., Cai, L., Abed-Meraim, F., 2020. Strain gradient crystal plasticity model based on generalized non-quadratic defect energy and uncoupled dissipation. Int. J. Plast. 126, 102617.
Lin, P., Liu, Z., Zhuang, Z., 2016. Numerical study of the size-dependent deformation morphology in micropillar compressions by a dislocation-based crystal plasticity model. Int. J. Plast. 87, 32–47.
Liu, D., Dunstan, D., 2017. Material length scale of strain gradient plasticity: a physical interpretation. Int. J. Plast. 98, 156–174.
Liu, D., He, Y., Dunstan, D.J., Zhang, B., Gan, Z., Hu, P., Ding, H., 2013. Toward a further understanding of size effects in the torsion of thin metal wires: an experimental and theoretical assessment. Int. J. Plast. 41, 30–52.
Logg, A., Mardal, K.-A., Wells, G., 2012. Automated Solution of Differential Equations by the Finite Element Method: the FEniCS Book. Springer Science & Business Media.
Lu, X., Zhang, X., Shi, M., Roters, F., Kang, G., Raabe, D., 2019. Dislocation mechanism based size-dependent crystal plasticity modeling and simulation of gradient nano-grained copper. Int. J. Plast. 113, 52–73.
Lu, X., Zhao, J., Wang, Z., Gan, B., Zhao, J., Kang, G., Zhang, X., 2020. Crystal plasticity finite element analysis of gradient nanostructured TWIP steel. Int. J. Plast. 130, 102703.
Middlemiss, R., Samarelli, A., Paul, D., Hough, J., Rowan, S., Hammond, G., 2016. Measurement of the Earth tides with a MEMS gravimeter. Nature 531, 614–617.
Miehe, C., Aldakheel, F., Mauthe, S., 2013. Mixed variational principles and robust finite element implementations of gradient plasticity at small strains. Int. J. Numer. Methods Eng. 94, 1037–1074.
Nielsen, K.L., Niordson, C.F., 2014. A numerical basis for strain-gradient plasticity theory: rate-independent and rate-dependent formulations. J. Mech. Phys. Solid. 63, 113–127.
Ottosen, N.S., Ristinmaa, M., 2005. The Mechanics of Constitutive Modeling. Elsevier.
Polizzotto, C., 2009. A nonlocal strain gradient plasticity theory for finite deformations. Int. J. Plast. 25, 1280–1300.
Ran, J., Fu, M., Chan, W.L., 2013. The influence of size effect on the ductile fracture in micro-scaled plastic deformation. Int. J. Plast. 41, 65–81.
Reddy, B.D., Ebobisse, F., McBride, A., 2008. Well-posedness of a model of strain gradient plasticity for plastically irrotational materials. Int. J. Plast. 24, 55–73.
Ryś, M., Stupkiewicz, S., Petryk, H., 2022. Micropolar regularization of crystal plasticity with the gradient-enhanced incremental hardening law. Int. J. Plast. 156, 103355.
Scherer, J.-M., Besson, J., Forest, S., Hure, J., Tanguy, B., 2019. Strain gradient crystal plasticity with evolving length scale: application to voided irradiated materials. Eur. J. Mech. Solid. 77, 103768.
Seungwoo, H., Taeok, K., Hakjoo, L., Hyunwoo, L., 2008. In: Temperature-dependent Behavior of Thin Film by Microtensile Testing, 2008 2nd Electronics System-Integration Technology Conference. IEEE, pp. 477–480.
Song, Y., Voyiadjis, G.Z., 2018. Small scale volume formulation based on coupled thermo-mechanical gradient enhanced plasticity theory. Int. J. Solid Struct. 134, 195–215.
Tajalli, S.A., 2020. A micro plasticity model for pure bending analysis of curved beam-like MEMS devices. Mech. Mater. 151, 103606.
Tang, H., Acharya, A., Saigal, S., 2005. Directional dependence of crack growth along the interface of a bicrystal with symmetric tilt boundary in the presence of gradient effects. Mech. Mater. 37, 593–606.
Tang, H., Choi, Y., Acharya, A., Saigal, S., 2004. Effects of lattice incompatibility-induced hardening on the fracture behavior of ductile single crystals. J. Mech. Phys. Solid. 52, 2841–2867.
Tang, X., Peng, L., Shi, S., Fu, M., 2019. Influence of crystal structure on size dependent deformation behavior and strain heterogeneity in micro-scale deformation. Int. J. Plast. 118, 147–172.
Velayarce, J.R., Zamanzade, M., Abad, O.T., Motz, C., 2018. Influence of single and multiple slip conditions and temperature on the size effect in micro bending. Acta Mater. 154, 325–333.
Voyiadjis, G.Z., Faghihi, D., 2012. Thermo-mechanical strain gradient plasticity with energetic and dissipative length scales. Int. J. Plast. 30, 218–247.
Voyiadjis, G.Z., Faghihi, D., Zhang, Y., 2014. A theory for grain boundaries with strain-gradient plasticity. Int. J. Solid Struct. 51, 1872–1889.
Wcisło, B., Pamin, J., 2017. Local and non-local thermomechanical modeling of elastic-plastic materials undergoing large strains. Int. J. Numer. Methods Eng. 109, 102–124.
Wheeler, J.M., Niederberger, C., Tessarek, C., Christiansen, S., Michler, J., 2013. Extraction of plasticity parameters of GaN with high temperature in situ micro-compression. Int. J. Plast. 40, 140–151.
Wu, X., Ramesh, K., Wright, T., 2003. The coupled effects of plastic strain gradient and thermal softening on the dynamic growth of voids. Int. J. Solid Struct. 40, 6633–6651.
Wulfinghoff, S., Böhlke, T., 2015. Gradient crystal plasticity including dislocation-based work-hardening and dislocation transport. Int. J. Plast. 69, 152–169.
Xiao, X., Chen, L., Yu, L., Duan, H., 2019. Modelling nano-indentation of ion-irradiated FCC single crystals by strain-gradient crystal plasticity theory. Int. J. Plast. 116, 216–231.
Zhang, H., Liu, J., Sui, D., Cui, Z., Fu, M., 2018a. Study of microstructural grain and geometric size effects on plastic heterogeneities at grain-level by using crystal plasticity modeling with high-fidelity representative microstructures. Int. J. Plast. 100, 69–89.
Zhang, L., Zhang, X., Song, J., Zheng, H., 2019. Thermal fracture parameter analysis of MEMS multilayer structures based on the generalized thermoelastic theory. Microelectron. Reliab. 98, 106–111.
Zhang, Z., Lunt, D., Abdolvand, H., Wilkinson, A.J., Preuss, M., Dunne, F.P., 2018b. Quantitative investigation of micro slip and localization in polycrystalline materials under uniaxial tension. Int. J. Plast. 108, 88–106.